Atmos. Chem. Phys. Discuss., 6, 6525–6585, 2006
www.atmos-chem-phys-discuss.net/6/6525/2006/

Atmospheric Chemistry and Physics Discussions

MIPAS level 2 operational analysis

P. Raspollini[1], C. Belotti[1], A. Burgess[6], B. Carli[1], M. Carlotti[2], S. Ceccherini[1], B. M. Dinelli[3], A. Dudhia[6], J.-M. Flaud[5], B. Funke[8], M. Höpfner[4], M. Lopez-Puertas[8], V. Payne[6], C. Piccolo[6], J. J. Remedios[7], M. Ridolfi[2], and R. Spang[7,*]

[1]Istituto di Fisica Applicata "N. Carrara" (IFAC) del Consiglio Nazionale delle Ricerche (CNR), Firenze, Italy
[2]Dipartimento di Chimica Fisica e Inorganica, University of Bologna, Bologna, Italy
[3]Istituto di Scienza dell'Atmosfera e del Clima (ISAC) del Consiglio Nazionale delle Ricerche (CNR), Bologna, Italy
[4]Forschungszentrum Karlsruhe GmbH, Institut für Meteorologie und Klimaforschung, Germany
[5]Laboratoire Interuniversitaire des Systèmes Atmosphériques (LISA) CNRS/ Univ Paris 12 et 7, France
[6]Atmospheric, Oceanic and Planetary Physics – Clarendon Laboratory – Oxford University, UK
[7]Earth Observation Science, Department of Physics and Astronomy, University of Leicester, UK
[8]Instituto de Astrofísica de Andalucía (CSIC), Granada, Spain
[*]now at: ICGI Forschungszentrum Jülich, Germany

Received: 15 February 2006 – Accepted: 10 March 2006 – Published: 13 July 2006

Correspondence to: P. Raspollini (p.raspollini@ifac.cnr.it)

Abstract

The MIPAS (Michelson Interferometer for Passive Atmospheric Sounding) instrument has been operating on-board the ENVISAT satellite since March 2002. In the first two years, it acquired in a nearly continuous manner high resolution (0.025 cm^{-1} unapodised) emission spectra of the Earth's atmosphere at limb in the middle infrared region. This paper describes the level 2 near real-time (NRT) and off-line (OL) ESA processors that have been used to derive level 2 geophysical products from the calibrated and geolocated level 1b spectra. The design of the code and the analysis methodology have been driven by the requirements for NRT processing. This paper reviews the performance of the optimised retrieval strategy that has been implemented to achieve these requirements and provides estimated error budgets for the target products: pressure/temperature, O_3, H_2O, CH_4, HNO_3, N_2O and NO_2, in the altitude measurement range from 6 to 68 km.

From application to real MIPAS data, it was found that no change was needed in the developed code although an external algorithm was introduced to identify clouds with high opacity and to exclude affected spectra from the analysis. In addition, a number of updates were made to the set-up parameters and to auxiliary data. In particular, a new version of the MIPAS dedicated spectroscopic database was used and, in the OL analysis, the retrieval range was extended to reduce errors due to uncertainties in extrapolation of the profile outside the retrieval range and more stringent convergence criteria were implemented.

A statistical analysis on the χ^2 values obtained in one year of measurements shows good agreement with the a priori estimate of the forward model errors. On the basis of the first two years of MIPAS measurements the estimates of the forward model and instrument errors are in general found to be conservative with excellent performance demonstrated for frequency calibration. It is noted that the total retrieval error is limited by forward model errors which make useless a further reduction of random errors. However, such a reduction is within the capabilities of MIPAS measurements, which

contain many more spectral signatures of the target species than what currently used. Further work is needed to reduce the amplitude of the forward model errors, so that the random error and the total error budget can be reduced accordingly.

The importance of the Averaging kernels for a full characterisation of the target products is underlined and the equations are provided for their practical applications.

1 Introduction

The MIPAS (Michelson Interferometer for Passive Atmospheric Sounding) instrument (Fischer et al., 2000, 2006[1]) is a Fourier transform infra-red spectrometer operating on board the environmental satellite ENVISAT launched by ESA on 1 March 2002. The first interferogram was measured on 24 March 2002 and from July 2002 nearly continuous measurements were obtained for the first two years of satellite operation. Due to problems with the mirror drive of the interferometer, MIPAS ceased measurements at the end of March 2004. Operations with reduced maximum path difference, corresponding to both a lower spectral resolution and a shorter measurement time, were resumed in January 2005. This paper concerns the higher spectral resolution measurements performed in the first two years of MIPAS operations.

The instrument is designed to perform measurements during both day and night for the determination, on a global scale, of the vertical profile of the Volume Mixing Ratio (VMR) of several atmospheric species relevant for the characterisation of the chemistry and climatology of the Earth's atmosphere. For this purpose, the spontaneous thermal emission of the atmosphere is observed in the middle infrared (from 685 cm^{-1} to 2410 cm^{-1}), a region containing a large fraction of the black body emission of the atmosphere as well as features due to the vibrational spectra of most atmospheric constituents. In the first two years of operation the spectral resolution of MIPAS was

[1]Fischer, H., Birk, M., Blom, C., et al.: MIPAS: an instrument for atmospheric and climate reasearch, Atmos. Chem. Phys. Discuss., in preparation, 2006.

0.025 cm^{-1} (defined as the spacing between independent spectral elements of the unapodized spectrum). This spectral resolution is sufficient to distinguish the majority of individual atmospheric spectral lines at high altitudes, although not high enough to resolve their shape, and is able to reduce significantly the apparent overlap of individual spectral lines at all altitudes where this is due to instrument lineshape.

In order to obtain the vertical distribution of minor atmospheric constituents with good vertical resolution, the observations are made of the limb of the Earth with an elevation pointing that can be varied in tangent altitude from 5 to 210 km and with an Instantaneous Field of View (IFOV) of 3×30 km^2 (vertical height times across-track width, at 10 km tangent altitude).

A spectrum at the maximum spectral resolution is obtained in 4.5 s. A limb sequence (or elevation scan) in the nominal observation mode is composed of 17 spectra that look at different tangent altitudes from 6 to 68 km and is acquired in 76.5 s. During each orbit, MIPAS performs 75 limb sequences plus measurements for instrument calibration ("space" view and internal blackbodies for offset and gain)

The operational analysis, performed by ESA, requires a robust code with no choice delegated to the operator and with the capability of Near Real Time (NRT) operation, that is with a distribution of the products within three hours from the measurement time. These requirements drive the analysis methodology and therefore the results reported here reflect the analysis and quality of operational data rather than the ultimate limit of MIPAS capabilities.

While the level 1 analysis (Nett and Perron, 2002a; Nett et al., 2002b; Perron et al., 2006[2]) determines, from the raw instrument data, the geolocated and calibrated spectra, the level 2 analysis determines, from level 1b calibrated spectra, the geophysical parameters of interest. This includes the pressure and temperature at tangent altitudes and the vertical profiles of six species selected to have highest priority, namely: O_3, H_2O, CH_4, HNO_3, N_2O and NO_2, in the altitude measurement range from 6 to

[2]Poulin, R., Aubertin, G., Perron, G., et al.: MIPAS Level 1B Algorithm Overview, Atmos. Chem. Phys. Discuss., in preparation, 2006.

68 km. These species are referred to as the target species.

The ESA operational level 2 code is based on a scientific prototype, named Optimised Retrieval Model (ORM), that was developed by an international consortium in the frame of an ESA Study. The ORM code is described in Ridolfi et al. (2000). The mathematical complexity of the inversion problem, combined with the large amount of data to be processed for each limb sequence in NRT, determines the challenging and conflicting requirements of an accurate and time efficient retrieval. An optimized retrieval strategy, combined with a series of mathematical and physical optimizations, was implemented in the ORM code.

The ORM code is also the prototype of the Off-Line (OL) level 2 processor that is used for the re-analysis of the measurements with improved geolocation and set up of the level 1 and level 2 chain. In the OL analysis the computing time constraint is relaxed by a factor of 2 in CPU processing terms allowing more iterations per retrieval and an extended range to be employed.

Given the novelty of the technical solutions implemented in the ORM, the assumptions and approximations adopted in this algorithm are critically discussed here in the light of MIPAS performance during the first two years of measurements and a review of the total error budget is provided. The choices associated with the new measurement scenario with reduced spectral resolution implemented after January 2005 will not be discussed in this paper.

This paper is also intended to provide a summary of the most important information that is necessary to the potential users of NRT and OL level 2 MIPAS operational products provided by ESA. In Sect. 2 the main features of the ORM are summarised, while the latest upgrades in both level 2 code and auxiliary data are described in Sect. 3. The different error sources in the forward model that affect accuracy of retrieved profiles are critically reviewed in Sect. 4 with the objective of assessing the correctness of the current estimation of the individual components. Averaging Kernels of the retrieved profiles are shown in Sect. 5. An assessment of the ORM performances, based on a statistical analysis of one year of measurements, is made in Sect. 6, and finally, in

Sect. 7, some examples of ORM products are shown.

2 Summary of ORM features

A detailed description of the ORM code is provided in Ridolfi et al. (2000), where also the pre-flight performances obtained with simulation tests are provided. For the benefit of the reader the main features of the ORM code are herewith briefly recalled.

The retrieval algorithm is based on the non-linear least-square fit (Menke, 1984; Sivia, 1998; Kalman, 1976; Rodgers, 2000) and consists of the global fit of a theoretical forward model calculation $\boldsymbol{F(p, x)}$ to the observations $\boldsymbol{y}$. $\boldsymbol{F(p, x)}$ simulates the observations starting from the quantities $\boldsymbol{x}$ to be retrieved and from a set of instrumental and geophysical parameters $\boldsymbol{p}$, that are considered to be known. The solution is found with an iterative procedure that uses the Gauss-Newton method, modified according to the Levenberg-Marquardt (Levenberg, 1944; Marquardt, 1963) criterion, for the minimisation of the χ^2 function. The χ^2 function is equal to:

$$\chi^2 = \boldsymbol{n}_{\text{iter}}^T \mathbf{V}_n^{-1} \boldsymbol{n}_{\text{iter}} \,, \tag{1}$$

where $\boldsymbol{n}_{\text{iter}} = \boldsymbol{y} - \boldsymbol{F}(\boldsymbol{p}, \boldsymbol{x}_{\text{iter}})$ is the vector of the residuals at iteration "iter", with $\boldsymbol{x}_{\text{iter}}$ equal to either the initial guess or the result of the current iteration, and $\mathbf{V}_n$ is the VCM (Variance-Covariance Matrix) of the observations.

At each iteration the unknown profile $\boldsymbol{x}_{\text{iter}}$ is given by:

$$\boldsymbol{x}_{\text{iter}} = \boldsymbol{x}_{\text{iter}-1} + \left(\mathbf{K}_{\text{iter}-1}^T \mathbf{V}_n^{-1} \mathbf{K}_{\text{iter}-1} + \lambda \mathbf{I} \right)^{-1} \mathbf{K}_{\text{iter}-1}^T \mathbf{V}_n^{-1} \boldsymbol{n}_{\text{iter}-1} \tag{2}$$

where $\mathbf{K}_{\text{iter}-1} = \frac{\partial \boldsymbol{F}(\boldsymbol{p}, \boldsymbol{x}_{\text{iter}-1})}{\partial \boldsymbol{x}_{\text{iter}-1}}$ is the Jacobian of the simulated radiance relative to the profile $\boldsymbol{x}_{\text{iter}-1}$, and $\mathbf{I}$ is the identity matrix. The Marquardt factor λ, that at each iteration is either increased or decreased depending on whether the χ^2 function increases or decreases, reduces the amplitude of the iteration steps and ensures that a stable convergence is reached.

At convergence it is assumed that a small value of λ is used and that its effect on the retrieval error can be neglected. In this case, we can define the solution matrix of the inverse problem or gain matrix as:

$$\mathbf{G} = \left(\mathbf{K}^T \mathbf{V}_n^{-1} \mathbf{K}\right)^{-1} \mathbf{K}^T \mathbf{V}_n^{-1} \tag{3}$$

and the errors associated with the solution of the inversion procedure can be characterised by the VCM of $\boldsymbol{x}$ given by:

$$\mathbf{V}_x = \mathbf{G}\mathbf{V}_n\mathbf{G}^T = \left(\mathbf{K}^T \mathbf{V}_n^{-1} \mathbf{K}\right)^{-1}. \tag{4}$$

Since the inversion is sufficiently well-conditioned, neither a priori information nor regularisation are applied.

The retrieval strategy adopted to handle the multiplicity of unknowns and the redundancy of the data is based upon the following three choices:

1. Sequential retrieval of the species
   The different unknowns are retrieved following a hierarchy of operations: first temperature and tangent pressures are retrieved simultaneously (henceforth denoted as the "p, T retrieval"), then VMR profiles of the target species are individually retrieved following the order of their reciprocal spectral interference, i.e.: H_2O first, followed by O_3, HNO_3, CH_4, N_2O and NO_2. The simultaneous p, T retrieval (see e.g. Carlotti and Ridolfi, 1999) exploits the hydrostatic equilibrium assumption that provides a relationship between temperature, pressure and geometrical altitude, the latter being determined by the engineering measurement of the pointing direction. Besides the target parameters, each retrieval also determines a frequency and altitude independent instrument zero-level offset and a frequency independent, altitude dependent absorption cross-section that models the atmospheric continuum and accounts for all the continuum-like emission effects that are not included in the line-by-line calculations.

2. Use of "microwindows"
   The retrieval is performed using a set of narrow (less than $3\,cm^{-1}$ width) spectral intervals, called "microwindows" (Dudhia et al., 2002a), that are selected as those intervals that contain the best information on the target parameters and are less affected by forward model errors, such as for instance uncertain spectroscopic data, interference of non-target species, Non-Local Thermal Equilibrium (NLTE) and line mixing effects.

3. Global fit analysis of the limb sequence
   The global fit approach (Carlotti, 1988) is adopted for the retrieval of each vertical profile. This means that the spectral data related to a complete limb sequence are fitted simultaneously. The global fit provides a full exploitation of the measurements and a rigorous determination of the correlation between atmospheric parameters at the different altitudes.

The core and the most time consuming part of the retrieval code is the forward model. A self-standing subroutine of the code, called OFM (Optimised Forward Model) performs this calculation. OFM computes the atmospheric radiance measured by the spectrometer as the result of the radiative transfer in a non-uniform medium as well as by the instrument effects. The OFM also computes the Jacobians with respect to the retrieved parameters.

Features that are taken into account are:

1. the effect of refractive index in the ray tracing of the optical path
2. Voigt profile for line shape modelling
3. use of a fine grid ($5{\cdot}10^{-4}\,cm^{-1}$) in the spectral domain for a monochromatic modelling of radiative transfer
4. convolution of the atmospheric spectrum with the Instrument Line Shape (ILS) and IFOV of the instrument.

On the other hand, NLTE effects, line mixing and pressure shifts have not been considered in the forward model, but are accounted for in the microwindow selection and in the error budget. The atmosphere is assumed horizontally homogeneous and in hydrostatic equilibrium.

Several mathematical and physical optimisations were studied to optimise the trade-off between accuracy and computing time. The main optimisations implemented in the OFM are:

1. definition of an appropriate sequence of operations that avoids the repetition of the same calculations and minimises the number of memorised quantities;
2. use for each species of cross-section look-up tables, that are compressed with the Singular Value Decomposition method (Dudhia et al., 2002b);
3. use of a pre-defined subset of the fine grid points of the spectral domain (irregular grid) for the computation of the fine grid spectra;
4. Curtis-Godson approximation for cross section calculation in order to reduce the vertical segmentation of the atmosphere;
5. analytical IFOV convolution performed using a polynomial approximation of the tangent altitude dependence of the spectrum (from a 2nd to a 4th order polinomium going from high altitudes to low altitudes);
6. analytical computation of derivatives;
7. apodization of the spectrum with the Norton-Beer strong (Norton and Beer, 1977) function. This is done in order to reduce the contribution of sidelobes of the lines lying outside the microwindow and hence limit the size of the spectral range in which the spectrum is calculated (typically an extension of $0.175\,cm^{-1}$ on both boundaries is considered).

Before ENVISAT launch, the optimised forward model was validated against an accurate Reference Forward Model developed at Oxford (Edwards, 1997). The retrieval code was validated both with self-consistency tests and against real measurements supplied by the MIPAS instrument on board of a stratospheric balloon (Friedl-Vallon et al., 2004), and by ATMOS measurements (Piccolo et al., 2004).

Both the forward and the retrieval model have participated in the intercomparison study with other retrieval codes in the frame of the AMIL2DA project (Clarmann et al., 2003c, a).

The performance of the MIPAS level 2 processor strongly depends on the used auxiliary data. For this reason in the following sub-sections the databases of auxiliary data used by MIPAS level 2 processor are described.

2.1 Spectroscopic database

A dedicated spectroscopic database is used for MIPAS experiment. It was built starting from the HITRAN96 database (Rothman et al., 1998, and http://www.hitran.com) with improvements obtained through new laboratory studies and new calculations. A first version of the MIPAS database, named "mipas_pf2.0", included updates for the HOCl, HNO_3, O_3, NO_2, CH_4 and H_2O molecules that were validated performing comparisons between atmospheric simulated spectra and atmospheric spectra measured by the ATMOS experiment that flew on the Shuttle (Piccolo et al., 2004). A new version of the spectroscopic database, named mipas_pf3.1 (Flaud et al., 2003b) was released after the launch and it was used for both the NRT and OL re-processing (starting with V4.59 of the ESA Instrument Processing Facility). Details of this version are provided in Sect. 3.2.

2.2 Reference atmosphere database

The MIPAS processing requires a climatology of profiles that are used for the determination of the initial guess of the retrieved species and to define the VMR of those

species that interfere with the analysed spectrum, but are not currently retrieved (interfering species). The initial guess of the retrieved species is obtained as a weighted mean of the profile retrieved at the previous limb sequence, if it exists, the ECMWF profile and the climatological one.

A seasonal climatology, referred to as the initial guess climatology (IG2), was constructed (Remedios, 1999) for temperature and 36 species on a 1 km grid from 0 to 120 km, mainly using a combination of observed satellite data (particularly from the UARS Reference Atmosphere project), tropospheric profiles from the MOZART model (Hauglustaine et al., 1998) and stratospheric profiles from the SLIMCAT model (Chipperfield, 1999). The seasons are three month periods, with mid-seasons of January, April, July and October arranged in six latitude bands per season (0–20°, 20–65°, 65–90° in each hemisphere). The trace gases included are: CO_2, O_3, H_2O, CH_4, N_2O, HNO_3, CO, NO_2, N_2O_5, ClO, HOCl, $ClONO_2$, NO HNO_4, HCN, NH_3, CFC11, CFC12, CFC14, CFC22, CCl_4, COF_2, H_2O_2, C_2H_2, C_2H_6, OCS, SO_2, SF_6, CFC13, CFC21, CFC113, CFC114, CFC115, CH_3Cl, N_2 and O_2.

In addition, five standard atmospheres were also produced to represent typical tropical, mid-latitude, polar summer and polar winter conditions. The principal purpose of these atmospheres was for use in development of cross-section look-up tables for the forward model, for microwindow selection and for error estimation where computing time was an issue. The standard atmospheres were also designed to capture the variability of the atmosphere and included one sigma, maximum and minimum profiles based on the data sources described for the IG2 atmosphere. The one sigma profiles were employed in the microwindow selection process (Sect. 2.3) and in the error estimation (Sect. 4) for the target species.

2.3 Microwindow database

Microwindows are subsets of the two-dimensional measurement domain of tangent altitude versus spectral channel. The selection algorithm is described in detail in Dudhia et al. (2002a) but, briefly, is based on minimising the total error defined as the sum of

the measurement error $\mathbf{V}_x$ (due to random noise, see Eq. 4) and various forward model errors:

$$\mathbf{V}_x^{\text{tot}} = \mathbf{V}_x + \sum_i \mathbf{V}_x^i \tag{5}$$

where each $\mathbf{V}_x^i$ represents an independent forward model error. The individual sources of these errors will be discussed in Sect. 4.

For each of these errors an error spectrum $\delta \boldsymbol{y}_i$ is computed as the difference between the forward model calculations obtained for a nominal value of the parameter and for the parameter perturbed by 1σ. The VCM of the forward model error in the measurement domain is given by:

$$\mathbf{V}_y^i = (\delta \boldsymbol{y}_i)\,(\delta \boldsymbol{y}_i)^T\,, \tag{6}$$

while the VCM in the retrieval domain is given by:

$$\mathbf{V}_x^i = \mathbf{G}\mathbf{V}_y^i\mathbf{G}^T \tag{7}$$

where $\mathbf{G}$ is the Gain Matrix used in the retrieval (see Eq. 3).

In order to provide a single set of microwindows which can be used globally, the actual minimised quantity represents a combination of the total errors evaluated for 5 different atmospheres covering a variety of atmospheric states (the standard atmospheres described in Sect. 2.2).

As well as determining the boundaries of the microwindow, the selection procedure allows spectral points within the microwindow to be "masked", i.e., excluded from the retrieval. This happens when the inclusion of the measurement would increase rather than decrease the total error or, in other words, the increase in forward model error outweights the decrease in random error.

This "negative information" concept is a direct consequence of the retrieval choices. Effectively, the microwindow selection attempts to minimise the impact of forward model errors allowing for the fact that the retrieval itself, with the minimisation of χ^2, will only

weight each measurement according to its random error contribution instead of the total error.

Figure 1 shows the locations of the microwindows used for the operational retrievals and compares them with the contribution of each species to the observed spectrum. The microwindows tend to be selected in spectral regions where the lines of the target molecule dominate (CO_2 is used in the case of the p,T retrieval). In Table 1 the complete list of nominal microwindows (i.e. those used in absence of both corrupted spectra and corrupted bands) are reported, together with their altitude range.

The retrieval is performed using a set of the "best microwindows". There is a limit after which no further microwindow can be added which reduce the total error of the selected set. However, the number of microwindows used in the operational processing of MIPAS data lies well inside this limit. Indeed, the limits of available computing power impose a time efficiency selection criterion within which a balance between random errors and forward model errors is sought.

The small number of microwindows and the use of spectral masks imply that only a few percent of the total number of measurements in each spectrum are actually used in the operational retrieval.

3 Post-launch upgrades

The preparatory studies lasted for about seven years and made possible the development of a quite reliable code. Indeed the analysis of the real MIPAS measurements indicated that only some minor upgrades in the level 2 processor were necessary. These have involved the pre-processor operations and the operating environment of the code defined by the input auxiliary data (including both retrieval settings and databases) and no change was made to the code itself. In the pre-processor a cloud filtering algorithm (see Sect. 3.1) was included to make the ORM more robust and the retrieved profiles more accurate.

For the input auxiliary data, a new version of the MIPAS dedicated spectroscopic

database was released (see Sect. 3.2), new convergence criteria were generated (see Sect. 3.3) and a revised retrieval altitude range was adopted (see Sect. 3.4). Some of these changes are related to a revision of the pre-flight choices that gave priority to the need to limit the computing time.

3.1 Cloud filtering

Shortly after launch, the new feature of the cloud filtering algorithm was introduced in the pre-processor of MIPAS level 2 code (Spang et al., 2004). Clouds have a very wide spectral signature and affect the measured spectra at all the wavelengths that are transparent to emission from the atmospheric layer containing the clouds. Both low resolution (cloud continuum) and high resolution features (line distortions due to scattering) can be observed at the spectral resolution of MIPAS (Greenhough et al., 2005; Spang et al., 2004; Höpfner et al., 2002); spectral bands may also be observed for polar stratospheric clouds (Spang and Remedios, 2003; Höpfner et al., 2005). This implies that on the one hand cloud information can be extracted from MIPAS measurements, but on the other hand spectra containing clouds can spoil the quality of the trace gas retrieval. Hence, clouds with high opacity must be identified and flagged so that retrievals of trace gas concentration are performed above the cloud top height. An example of the global cloud top height map obtained from the analysis of 3 days of MIPAS measurements from 15 September 2002 is shown in Fig. 2. The highest cloud heights are found, as expected, in the tropical upper troposphere (sub-visible cirrus) and in the Antarctic polar vortex (polar stratospheric clouds). The polar stratospheric clouds in this period were the final ones observed prior to the unusually early break-up of the vortex in that year (see also Sect. 8).

The cloud detection algorithm consists of a threshold test applied to the ratio of the integrated signal in two microwindows (Spang et al., 2002), originally defined within what is Band A (685–970 cm^{-1}) of the MIPAS instrument. Subsequent calculations with the Oxford Reference Forward Model identified useful cloud microwindow pairs in Band B (1215–1500 cm^{-1}) and D (1820–2410 cm^{-1}); no such pairs could be de-

termined in Bands AB (1020–1170 cm^{-1}) and C (1570–1750 cm^{-1}). As implemented for MIPAS processing, the cloud detection scheme is arranged hierarchically so that the primary cloud test, which operates between 6 and 45 km, is performed with the Band A pair of microwindows. Clouds are flagged if the ratio of radiances between microwindow 1 (788.2–799.25 cm^{-1}) and microwindow 2 (832.3–834.4 cm^{-1}) is less than 1.8 between 6 km and 45 km; the upper limit of microwindow 1 can also be set to 796.25 cm^{-1} (Spang et al., 2002) which allows slightly more cloud sensitivity and is likely to be implemented for MIPAS in future processing. The thresholds for bands B and D are currently set to 1.2 and 1.8, respectively.

The determination of whether the line of sight is seriously affected by clouds and the consequent removal from the retrieval process of this line of sight (cloud filtering) was found to be an important operation. Firstly, it directly removed the anomalous mixing ratios that result from retrievals made with cloud-contaminated spectra. Secondly, it reduced the instabilities of the convergence process and improved the quality of MIPAS products above the clouds. At the same time, the scheme allows for the possibility that trace gas concentrations can still be retrieved for clouds or aerosol layers with low opacity in the infrared.

3.2 Spectroscopic database

After launch, version "mipas_pf3.1" (Flaud et al., 2003b) of the MIPAS dedicated spectroscopic database was released. It contains some improvements with respect to "mipas_pf2.0" based on both new laboratory spectroscopy and new calculations (Flaud et al., 2003a, c). The improvements concern the following molecules: CO_2, HNO_3, CH_4, NO_2, O_3 and COF_2.

In particular, the new spectroscopic data for HNO_3 are responsible of a change of about 14% in the retrieved HNO_3 VMR (Flaud et al., 2003a, b; Mencaraglia et al., 2006).

In Fig. 3 the measured wide band spectrum relative to the spectral interval of band

A between 820 and 970 cm^{-1} containing four HNO_3 bands (two interacting HNO_3 cold bands ν_5 and $2\nu_9$ centered at 879.109 and 896.448 cm^{-1}, respectively, and two hot bands $\nu_5-\nu_9+\nu_9$ and $3\nu_9-\nu_9$ located at 885.424 and 830.6 cm^{-1}, respectively) is compared with the corresponding simulated spectrum (computed using the retrieved profiles and the "mipas_pf3.1" spectroscopic database) in the case of a limb measurement at 24 km tangent altitude. Also the residuals and the measured NESR (Noise Equivalent Spectral Radiance) are reported. Residuals are consistent with the NESR level with no strong feature larger than the noise, proving that a good agreement is obtained between measurements and forward model calculations also for wide-band spectra.

3.3 Retrieval range

In the altitude domain, ORM determines discrete values of the VMR in correspondence of the measured tangent altitudes (or of a subset of them). In the nominal measurement scenario MIPAS measurements extend from 6 to 68 km, but the level 2 retrieval can be limited to a selected molecule dependent altitude range (retrieval range). For the first post-launch operations the choice was made to limit the retrieval range to those altitudes in which good retrieval accuracy was found to be possible with pre-flight tests. Before the implementation of the cloud filtering, the preliminary retrieval range did not extend below 12 km because of the high probability of cloud occurrence below this altitude. Above the highest point and below the lowest point of the retrieved profile the shape of the profile is assumed to be equal to that of the initial guess profile and the fit just applies a scaling factor that avoid discontinuities and preserves the shape of the initial guess profile. This may introduce a bias in the highest and lowest points of the retrieved profile which depends on the assumed shape of the profile.

Tests performed after the ENVISAT launch proved the criticality of the adopted extrapolation strategy. Moreover the analysis of real data highlighted the need to extend the retrieval range of NO_2 at higher altitudes to account for its increase during the polar night.

In order to overcome the approximations introduced by the extrapolation strategy and also to exploit the downward extension to 6 km made possible by the use of cloud filtering, the strategy adopted for the definition of the retrieval range was changed to include all the points that are useful for improving the overall quality of the retrieval, independently of the quality attained at that specific altitude. The extension of the retrieval range does not imply that the added retrieved points are always useful geophysical data. As it will be explained in Sect. 6, indications on the usefulness of retrieved data can be provided by the Averaging Kernel Matrices. For istance it has been found that the additional points retrieved by the OL analysis for H_2O and NO_2 (namely 68, 9 and 6 km for H_2O and 68 and 60 km for NO_2) are not expected to have a physical meaning and the values retrieved at these altitude points are reported as part of the MIPAS products for their mathematical value only (they are the values used by the retrieval for modelling the overall profile).

The extension of the retrieval range implies an increase in the processing time, and hence this improvement is only implemented in the OL products, while the NRT products are still obtained using the preliminary retrieval range.

The retrieval ranges for the different species are listed in Table 2 for both the NRT and the OL cases.

3.4 Convergence criteria

The retrieval is performed through an iterative procedure aimed at reaching the minimum of χ^2. The convergence criteria determine when the iterative procedure stops.

The convergence criteria adopted in the MIPAS level 2 processor are based on three conditions:

1. Linearity of the inversion problem. The maximum relative difference between the χ^2 projection made at the previous iteration on the basis of the linearity assumption and the real χ^2 is less than a pre-defined threshold T_1.

2. Attained accuracy. The maximum relative variation (in two subsequent iterations) of the fitted parameters is less than a pre-defined threshold T_2.

3. Computing time. Due to general computing time constraints in MIPAS level 2 processor, there is a maximum number of allowed iterations.

The retrieval is stopped if one of the above 3 conditions is fulfilled, the convergence is reached if one of the first two conditions is fulfilled.

Tests performed after ENVISAT launch showed the criticality of the convergence criteria thresholds. If, in order to reach convergence with a small number of iterations, the thresholds used for convergence criteria are not sufficiently stringent, the convergence error, defined as the difference between the profile at convergence and the profile obtained after a sufficiently large number of iterations, may be comparable with the random error.

In general with more stringent thresholds a greater number of iterations is needed, with a consequent increase in computing time. As a consequence, more stringent thresholds are used only for the computation of the OL products.

It has been observed that in order to reduce the convergence error, the criterion on the maximum variation of the retrieved parameters has to be made more active than the criterion on linear variation of χ^2. This is obtained by using in the OL auxiliary data very stringent T_1 values with respect to T_2 values. Typical T_1 values in NRT auxiliary data are less than 0.15, while OL T_1 values are less than 0.02. The NRT T_2 values are 0.01, while OL T_2 values are less than 0.2. Furthermore, the maximum number of iterations was reduced to 8 in the OL case from the value of 10 in the NRT case, since it was verified that typically 3–6 iterations are sufficient to reach convergence. Scans that do not reach convergence in 8 iterations are generally critical, and it was decided not to waste time for them.

The convergence criteria adopted for OL products make the convergence error small enough to be neglected in the total error budget, while in NRT products the convergence error may be comparable with the random error.

4 Assessment of total error budget of retrieved profiles

As shown in Eq. (5), the total error budget of the retrieved profiles includes two contributions: the measurement error and the forward model errors.

The measurement error is due to the mapping of random radiometric noise into the retrieved profiles. The VCM $\mathbf{V}_x$ of the noise error is computed by ORM using Eq. (4). The VCM of the observations $\mathbf{V}_n$, that appears in that formula, is calculated using the radiometric noise (expressed in terms of Noise Equivalent Spectral Radiance NESR) provided by level 1 processor, and takes into account the correlation between spectral points due to the apodization process. MIPAS in-flight radiometric noise is in general better than the requirements with the only exception of the boundaries of the measured spectral region, below 700 cm^{-1} and above 2300 cm^{-1} (Nett et al., 2002b).

The forward model errors are due to uncertainties in instrument characterisation and in input parameters of the radiative transfer, as well as to approximations in the forward model itself. The forward model errors are determined on the basis of a priori estimates of these uncertainties. The sources of forward model errors which have been considered are listed in Table 3 together with their assumed amplitudes.

After ENVISAT launch a dedicated analysis was performed with ORM to assess the correctness of the a priori estimate of these errors. In this section the results of the ORM tests, as well as findings from other external tests, are reviewed in order to verify the estimation of each error component of the total error budget.

The square roots of the diagonal elements of all matrices involved in Eq. (5) for mid-latitude day-time conditions are shown for the various MIPAS products in Figs. 4 and 5. The random noise varies from measurement to measurement. The values shown in Figs. 4 and 5 (denoted by RND) are based on in-flight values of NESR from orbit 2081.

From these figures it emerges that the forward model error contribution is comparable with the measurement error. As the forward model errors are better understood they can be reduced and a new microwindow selection can be performed for an equal reduction of the measurement error and of the total error budget. A significant amount

of work is in progress in this direction. Presently the total error is larger than the proposed objectives of the mission and significantly larger than what can be potentially obtained from the wide spectral coverage of MIPAS measurements.

4.1 Error in instrument characterisation

Instrument effects are modelled in the forward model and approximations in the instrument characterisation can be a source of error. ORM has the capability of retrieving, together with the target parameters, also some parameters related to instrument effects such as frequency calibration, width of ILS and radiometric calibration. The retrieval of these non-target parameters has allowed a validation of the instrument characterisation and an assessment of the correctness of instrument error estimates.

4.1.1 Radiometric gain

Radiometric accuracy is crucial because it directly affects the accuracy of temperature and VMR retrievals. The high correlation between radiometric accuracy and retrieved parameters makes it difficult to extract information on radiometric accuracy from the level 2 analysis. Investigations performed on dedicated measurements for the instrument characterisation have proved that the radiometric errors are within the specifications of MIPAS instrument performance (Birk and Wagner, 2002; Nett et al., 2002b). However, tests performed on the measured integrated radiance highlighted for some bands the presence of an oscillation in the gain calibration. The oscillation is correlated with the forward/reverse direction of the sweep and is more evident in those bands in which a non-linearity correction has to be applied to the detectors. This oscillation, even if within the requirements, seriously affects the level 2 analysis because it enhances the anticorrelations that exist between retrieved values at contiguous altitudes and induces an oscillation in retrieved profiles. Forward-reverse oscillations have been significantly reduced with an improved non-linearity correction in level 1 processor and the residual effects that are present in the radiance cause an error in the retrieved

profiles that is smaller than the mean random error.

In conclusion, the investigations on radiometric accuracy have shown that the instrument performance is within the requirements, and also the amplitude attributed to the radiometric gain error component, which is based on the requirements, is correct.

4.1.2 Spectral calibration

Tests performed by ORM to validate the spectral frequency calibration of level 1 processing were made with the fit of a frequency dependent and altitude independent frequency scaling factor for all target species. From the analysis of the frequency dependence of the frequency scaling factor it was found that, while level 1 processor assumes that the frequency dependence can be modelled with a slope, the dependence on frequency is better modelled by a slope and a quadratic term. This systematic difference is now corrected in the level 2 pre-processor.

Concerning the time dependence of the frequency scaling factor retrieved by ORM, Fig. 6 shows its deviation from unity as a function of the limb sequence index for a full orbit. This plot was obtained after the correction of the frequency dependence described above. The curves in the plot are grouped with different colours according to the number of spectral points used for the retrieval. Since a larger number of spectral points provide a better accuracy, the scattering of the retrieved values is reduced when more points are used (see blue curves). The spread of the curves (about 3 parts in 10^7) gives an idea of the attained frequency calibration accuracy, that is better than the MIPAS requirement (equal to $1{\cdot}10^{-6}$ cm^{-1}). A degradation of the performance is visible only in the first 3 scans of the orbit, characterised by large values of the frequency scaling factor. This is due to the use in level 1 processor of an approximated default calibration for those sequences that are analysed before the first frequency calibration measurement is made.

On the basis of these tests, we can conclude that the amplitude attributed to this error component ($\Delta\sigma/\sigma$ =0.001) is conservative. However, as it can be observed in Figs. 4 and 5, this error is usually a small contribution to the total error budget. Indeed

a frequency shift causes both a positive and a negative residual of the two sides of a line, which increases the value of the χ^2, but has only a small effect on the value of the fitted intensity.

4.1.3 Width of the apodized instrument line shape

The Apodized Instrument Line Shape (AILS) is equal to the convolution of the ILS determined by the level 1 processor with the apodization function adopted in the level 2 analysis. The width of the AILS is dominated by the width of the apodization function, but a correct modelling of the ILS is important because a small error in the ILS, even if it does not change significantly the AILS and the residuals, can cause a large variation of the χ^2. This is explained by the fact that correlations are taken into account for the calculation of the χ^2 (see Eq. 1) and the errors caused by the ILS, even if damped by the operation of apodization, are properly determined.

The ORM is able to fit a band dependent and altitude independent ILS broadening correction. A broadening correction that is practically equal to zero is retrieved. This, together with the low values of the χ^2, indicates that the ILS width is determined in level 1 with an accuracy of about 0.2%. On the other hand a different result is obtained from a statistical analysis of the observed residuals, performed on the first two years of MIPAS measurements. In general this analysis consists in the fit of the residuals with the error spectra associated to each error and is named Residual and Error Covariance (REC) analysis (Dudhia, 2002). For the analysis of the ILS width error, the residuals are fitted with the second derivative of the spectrum and a correlation of about 2% between the residual and the second derivative of the spectrum is found. This empirically detected second derivative error is referred to as ILS width error even if causes different from ILS modelling may be responsible for it. Further investigations are on-going.

4.2 Errors in radiative transfer parameters

Investigations have been made to check the correctness of the uncertainties in the input parameters of the forward model with respect to their assumed variability. Results are summarised below.

4.2.1 Interfering species

Each target species is retrieved by ORM with an individual fit in which all other interfering species are known parameters. For the interfering target species, whenever available, the profile retrieved in the previous fit is used and, for all other interfering species, the assumed profile is given by the climatological database described in Sect. 2.2.

The uncertainties associated with the climatological profiles are the climatological 1-σ variabilities taken from extreme concentration profiles (Remedios, 1999) for each of the standard conditions (tropical, mid-latitude day/night, polar winter and polar summer). Concerning the contaminant species which are retrieved by MIPAS in a prior retrieval step, the retrieval total error of 10% is assumed.

The errors induced by the interfering species was verified with the REC analysis which has highlighted that the profile of some non-target species (COF_2, HOCl, H_2O_2 and NH_3) differs from the climatological profile more than climatological variability and the variability of some other non-target species (HCN, HNO_4) is underestimated. However, none of these deviations affects significantly the error budget. An upgrade is probably needed for the variability of SO_2: the REC analysis indicates SO_2 variability much smaller than assumed by the climatological variability. This is due to climatological variability allowing for volcanic activity whereas during MIPAS operation there has been no significant eruption affecting stratospheric SO_2. A reduction in climatological variability by a factor 10 is recommended since this is currently a significant component of the error budget for CH_4.

4.2.2 Shape of profile outside retrieval range

As described in Sect. 3.3, ORM assumes a fixed-shape of the atmospheric profile above the highest and below the lowest retrieval levels. The error due to this approximation has been recently included in the total error budget and is a significant error component at high altitudes. The NO_2 retrieval is particularly affected by this error, due to the diurnal variability of this species and to the large variability of the profile with season and latitude. The extension of the retrieval range, implemented in the OL products, effectively reduces this error.

The error due to the assumption of a fixed shape of atmospheric profile outside the retrieval range is calculated assuming that the "true" profile can deviate by climatological variability. No significant discrepancies have been highlighted in the climatological variability of the target species at high altitudes, and hence this error is now adequately accounted for.

4.2.3 Spectroscopic database errors

The spectroscopic database errors are due to uncertainties in the strength, position and width of infrared emission lines. The spectroscopic error estimates reported in Figs. 4 and 5 are based on uncertainty parameters relative to previous versions of the spectroscopic database. In the mipas_pf3.1 release of the MIPAS dedicated spectroscopic database these error estimates have been re-estimated and have mostly been reduced. The errors have been estimated at best using the available experimental data and/or calculations, but it is worth stressing that this is a difficult problem given the fact that in a number of papers no real estimation of the various errors is performed. Hence the spectroscopic errors reported in Figs. 4 and 5 are most likely conservative. Further information on the MIPAS spectroscopic database updates can be found in two technical reports (Flaud and Piccolo, 2001, 2003).

4.2.4 Temperature and tangent pressure propagation error

The pointing of the instrument is a very critical quantity in the level 2 analysis of limb measurements. In order to compensate for bias angles and harmonic pointing variations during the orbit, the Line-of-Sight is determined with in-flight calibrations made viewing at stars. Tests performed after launch (Clarmann et al., 2003b) showed that in the first few months of operations the MIPAS engineering tangent altitude had a bias of up to 3 km, but after an upgrade of the MIPAS pointing system the bias was reduced within the accuracy specification, i.e. 900 m. The short term pointing stability, during one interferometer sweep of 4 s duration, was verified to be better than 80 m (Ridolfi, 2005).

In order to further reduce the effect of the instrument pointing bias on retrieved profiles, the tangent pressures are fitted as part of the p, T retrieval. The short term pointing stability is exploited to improve the p, T retrieval with the hydrostatic equilibrium constraint that is obtained with the altitude increments of the engineering pointing. The retrieval of the tangent pressure is estimated to have an accuracy of about 1% which corresponds to an altitude uncertainty of about 70 m.

Neverthless, the altitude grid, that is derived from the pressure grid using the hydrostatic equilibrium and the lowest tangent altitude as a starting point, is affected by a total error larger than the retrieved tangent pressure.

Indeed the large bias (3 km in the early measurements and 900 m in the recent measurements) in the absolute value of the engineering tangent altitude induces a shift in the whole tangent altitude grid. For this reason it is preferred to represent the retrieved profiles as a function of pressure grid, which is an accurate retrieved quantity, and not as a function of the altitude grid, which is affected by the bias of the engineering pointing.

A pointing jitter was also detected in level 1 analyses of the un-decimated interferogram[3]. Tests made on the measured spectra have shown that no ghost is visible above

[3] M. Birk, private communications

the measurement noise and, because of the random phase of this jitter, also averaged spectra do not show the effect. This error is being monitored, but, because of its small amplitude, is presently not included in the forward model error budget.

Tangent pressure and temperature, which are simultaneously retrieved because of the large correlation that exists between the two parameters, are an important cause of error in VMR retrievals.

These errors are computed a posteriori using the propagation matrix **E** providing the mapping of p, T error on the retrieved VMR profiles:

$$\mathbf{V}_{xPT} = \mathbf{E}\mathbf{V}_{PT}\mathbf{E}^T, \tag{8}$$

where $\mathbf{V}_{xPT}$ is the VCM of the p,T induced error on the VMR profile and $\mathbf{V}_{PT}$ is the VCM of the p,T retrieval. In general this operation has to be performed for both the measurement error and the forward model components of p, T error. In Figs. 4 and 5 only the measurement error is included in the estimate of this error component.

In general matrix **E** depends on the set of microwindows used for VMR retrievals and on the atmospheric status (temperature and VMR profiles). However, it has been verified (Raspollini and Ridolfi, 2000) that in practice the dependence on the atmospheric status can be neglected.

A set of pre-tabulated propagation matrices has been computed for the mid-latitude standard atmosphere for the nominal set of microwindows.

4.3 Deficiencies in the radiative transfer model

The forward model computation is the most time consuming part of the retrieval code. Time efficiency is obtained by means of both physical and mathematical optimisations, as well as the use of microwindows that makes possible to neglect some effects.

The results of the tests aimed at verifying the correctness of the assumptions are discussed below.

4.3.1 Line-mixing

Line mixing (Edwards and Strow, 1991; Rosenkranz, 1975) corresponds to the deviation of the measured line shape from the Voigt function, occurring when collisions between a radiating molecule and the broadening gas molecules cause the transfer of population between different ro-vibrational states. Line mixing affects especially the Q-branches where transitions between ro-vibrational energy levels closer than $K_B T$ (K_B is the Boltzmann constant, T is the temperature) are packed together. The most apparent effect of line-mixing is a reduction of the cross-section in the wings of the branch.

Line mixing is neglected in the forward model, but the error of this approximation is taken into account in the microwindow selection.

An investigation was performed on four microwindows selected for p,T retrieval that are most affected by line-mixing, namely 728.3–729.125 cm^{-1}, 741.975–742.250 cm^{-1}, 791.375–792.875 cm^{-1}, 763.375–766.375 cm^{-1}. The analysis consisted of the comparison of the averaged residuals with the expected line mixing error spectra. A clear correlation between averaged residuals and line mixing error is noticed, but in general the averaged residuals are smaller than the error spectra indicating that a safe overestimate of the error has been adopted.

In some microwindows the error due to line-mixing is locally comparable with the random error of the single measurement, because the microwindow selection allows this occurrence when positive and negative errors compensate each other.

We conclude that the line-mixing effect is based on a correct model and is correctly taken into account in the microwindow selection.

4.3.2 Horizontal homogeneity assumption

The atmosphere sounded by MIPAS is assumed to be horizontally homogeneous. The extension of the atmospheric region observed with limb sounding geometry can reach a length approaching 2000 km. As a consequence, the homogeneity assumption can be critical in presence of pronounced horizontal structures in the atmosphere as en-

countered while crossing the terminator for photochemically active species, or the polar vortex in ozone-hole conditions.

In order to verify the impact of the homogeneity assumption, ORM results were compared with those obtained by the GEOFIT retrieval algorithm (Carlotti et al., 2001) that performs the simultaneous retrieval of all the observations acquired along a full orbit and accounts for the horizontal inhomogeneities.

Differences between the results of the two retrieval codes may be larger than the random error bars, but they are not correlated with the horizontal variability of the atmosphere. Therefore the observed differences are to be attributed to the differences between the two models rather than the horizontal homogeneity assumption in the ORM and it was not possible to provide an experimental constraint to the amplitude of this error. Simulations have shown that gradients in temperature can be the largest source of error among all gradients. In Figs. 4 and 5 a conservative estimate of a gradient of 1 K/100 km is made and in general a much smaller error is expected.

4.3.3 Local Thermodynamic Equilibrium assumption

The inclusion of non-LTE emission effects into an operational retrieval algorithm has a high cost in computation time and requires a major effort for modelling and coding all non-LTE processes. However, MIPAS measurements are mostly concentrated in the stratosphere, where the non-LTE effects are generally weak. Furthermore, MIPAS has a high spectral resolution and a wide spectral coverage which enables the selection of ro-vibrational lines of the bands less affected by non-LTE. For these reasons non-LTE modelling was not included in the operational retrieval algorithm and the microwindows selection is made taking into account the non-LTE errors. The non-LTE errors are estimated from pre-tabulated error propagation matrices which reflect the linear response of the retrieval to perturbations calculated from the difference of Non-LTE and LTE synthetic spectra. Several models are used for the computation of the non-LTE populations of all the relevant species (including also gases not being retrieved operationally but potentially contaminant, such as CO and NO). A detailed description of

the non-LTE models and the species and emitting levels for which non-LTE populations are computed can be found in Clarmann et al. (1998) and in a subsequent update by Lopez-Puertas et al. (2002).

The evaluation of the non-LTE effects requires independent measurements from a "non-LTE free" instrument. Such measurements were not available in the case of MIPAS pressure and temperature. However, the good agreement found between the temperatures retrieved from the SABER 15 μm emission measurements, using a non-LTE model for the CO_2 bands very similar to that used in the microwindows selection mentioned above, with rocket in situ measurements and with ground-based lidar measurements (Garcia-Comas et al., 2003; Mertens et al., 2006[4]) gives us confidence in the CO_2 non-LTE model. Non-LTE retrievals, performed from MIPAS data using the operational microwindows in the 15 μm fundamental bands and the non-LTE model mentioned above, have shown that non-LTE effects in temperature are smaller than 0.5 K below 60 km for all conditions, except in the lower mesosphere when it is significantly warm, e.g., polar winter or stratospheric warming. In these cases LTE retrievals may underestimate the temperatures by 1 to 3 K in the 50–70 km region. In daytime conditions, temperature could be overestimated by 1 to 2 K at altitudes from 60 to 70 km.

Concerning O_3, non-LTE retrievals of O_3 from the MIPAS upper atmosphere data in the altitude range from 20 to 100 km have been compared with "non-LTE free" stellar occultation GOMOS measurements (Verronen et al., 2005) and an agreement within 10–15% is obtained in the stratosphere and lower mesosphere. These MIPAS retrievals use the same emitting lines from the 14.8 μm and 10 μm fundamental bands as the operational retrieval, and the same non-LTE model that is used in the microwindow selection. Non-LTE retrievals performed using these microwindows show that non-LTE

[4] Mertens, C. J., Russell III, J. R., Mlynczak, M. G., She, C.-Y., Schmidlin, F. J., Goldberg, R. A., López-Puertas, R. A., Wintersteiner, P. P., Picard, R. H., Winick, J. R., and Gordley, L. L.: Retrieval of kinetic temperature and carbon dioxide from broadband infrared limb emission measurements taken from the TIMED/SABER instrument, Adv. Space Res., submitted, 2006.

effects in operational O_3 are negligible in the whole altitude range and conditions, except above 55 km in the polar winter-like conditions (warm lower mesosphere), where ozone can be underestimated by 10–15%.

The evaluation of non-LTE effects in the retrieval of water vapour is complicated by non-linear radiative transfer due to saturation effects in the fundamental (010→000) band used for the retrieval in the upper stratosphere. Non-LTE model errors in retrieved H_2O profiles can thus have different sign and altitude dependence than in the linear case. A recent study[5] shows that although vibrational temperatures of the 010 state depart from LTE generally above 60 km, mesospheric non-LTE emissions can enhance measured daytime radiances up to 10% at tangent heights around 50 km and 20% at 60 km due to solar excitation. The same study[5] demonstrates that the collisional rates used in the H_2O non-LTE modelling for the MIPAS non-LTE error assessment reproduce the Non-LTE effects measured by MIPAS itself.

The estimated non-LTE model error for H_2O retrieval varies from less than 5% during night below 50 km to 30% at 60 km during day time. A comparison of retrieved day and nightime H_2O (see Fig. 7) reveals systematic daytime enhancements of 5–10% in the 2000–2700 K (50–60 km) region while above, H_2O is up to 30% lower at daytime than at nighttime. These day/night differences can be attributed to non-LTE retrieval errors as it has been demonstrated by retrieving H_2O under assumption of LTE conditions from simulated spectra (Clarmann et al., 2003a). In any case, these non-LTE errors are within the limits of the estimated error budget.

Experimental evidence for non-LTE effects in CH_4 emissions in the ν_4 band was found by López Puertas et al. (2005). Non-LTE minus LTE limb radiance differences have been detected above 45 km, increasing up to 20% at 60 km. This study demonstrated that the non-LTE model used for the non-LTE model error assessment of MIPAS CH_4 fully reproduces the observed non-LTE features. The estimated non-LTE model errors are less than 2% below 50 km and larger than 20% at 60 km. These values are also in consonance with the day/night differences of three month means of retrieved

[5] Koukouli et al., private communication

CH_4 (see Fig. 8). Higher daytime CH_4 (5–10%) is retrieved above about 45 km (potential temperature of 1700 K) under LTE assumption due to population enhancements by solar excitation.

Possible non-LTE effects in the retrieval of N_2O have been estimated on the basis of theoretical non-LTE population calculations which indicate non-LTE-induced deviations of less than 1% for retrieved N_2O. No evidence of non-LTE effects in N_2O emissions has been found so far. Also, day/night differences of 3 month mean retrieved N_2O (see Fig. 9) do not hint at systematic deviations due to non-LTE neglect in the retrieval.

Non-LTE effects in the 6.2 μm region used for the retrieval of NO_2 have been analysed in detail by Funke et al. (2005). Non-LTE effects in retrieved NO_2 cannot be evaluated by means of day/night differences due to diurnal variations of this key species.

The chemical excitation rate of the NO_2 ν_3 states emitting in this spectral region were found to be 50 times less than estimated in previous studies. In the study of Funke et al., the non-LTE retrieval of NO_2 was performed using the updated rates and results were found to be in good agreement with non-LTE-free HALOE data. These new rates have also been incorporated in the assessment of non-LTE errors in the ORM retrieval of NO_2. No significant error is expected below 50 km. Above, the LTE assumption leads to an underestimation of NO_2 by 10–50% with highest deviations at polar winter conditions.

5 Computation of the total error of retrieved profiles

According to Eq. (4), the total error is obtained as a quadratic sum of measurement and forward model errors. The different components of this budget can be acquired from different sources.

The measurement error $\mathbf{V}_x$ is computed by level 2 processor and is reported in the level 2 output files.

The forward model errors $\mathbf{V}_x^i$, of which only the diagonal elements are provided, are available at http://www-atm.physics.ox.ac.uk/group/mipas/err. In this database, esti-

mates are given for the five standard atmospheres.

It has to be noticed that the error in VMR profiles due to the propagation of p and T errors, which is reported in the above data base, does not include the effect of forward model errors in p and T retrieval and does not account for the variability of the p, T retrieval errors. For a more accurate estimate of the p, T error propagation it is necessary to propagate, according to a suitable propagation matrix **E** as described in Sect. 3.2.4, the total error budget of the individual p, T retrievals into the VMR retrieval.

The propagation matrices **E** for the different species are included in the level 2 auxiliary data set and are available at http://www.ifac.cnr.it/retrieval/Auxiliary.html.

Access to the individual contribution allows, when necessary, to separate the random and systematic components of the error budget. Indeed, most of the forward model errors can be either random or systematic according to the ensemble of measurements that is being considered.

6 Averaging kernels

For a full characterisation of the retrieved profiles, along with the error information it is necessary to know how the description of the true state of the atmosphere is affected by the observing system. This information is provided by the averaging kernel matrix (AKM) and is indispensable for the validation operations when comparison between different measurements with different vertical resolution of the same atmospheric vertical profiles are performed (Ceccherini et al., 2003; Rodgers and Connor, 2003; Ridolfi et al., 2006). It is also required for comparisons to models with higher vertical resolution than MIPAS.

In the linear approximation, the relation connecting the retrieved profile with the true state of the atmosphere is given by:

$$\hat{\boldsymbol{x}} - \hat{\boldsymbol{x}}_0 = \mathbf{A}\,(\boldsymbol{x} - \boldsymbol{x}_0)\,, \tag{9}$$

where $\hat{\boldsymbol{x}}$ is the retrieved profile when the true state of the atmosphere is $\boldsymbol{x}$, $\hat{\boldsymbol{x}}_0$ is the

retrieved profile when the true state of the atmosphere is the linearization state $\boldsymbol{x}_0$ and $\mathbf{A}=\left.\frac{\partial \widehat{\boldsymbol{x}}}{\partial \boldsymbol{x}}\right|_{\boldsymbol{x}_0}$ is the Averaging Kernel Matrix.

The rows and the columns of **A** are respectively the averaging kernels (AK) and the delta-function responses. There is one AK for each retrieved parameter and one delta function for each grid point used to represent the AKs. The AKs are in general functions peaking at the grid point that coincides with the altitude of the retrieved parameter and have a width that is a measurement of the vertical resolution of the retrieved parameter. When the grid used for the representation of the AKs concides with the altitudes of the retrieved parameters (measurement grid) and no a-priori information is used for the retrieval, **A** is the identity matrix.

In the case of MIPAS no a priori information is used and **A** differs from the identity matrix only when a fine grid is used for the representation of the AKs. The fine grid is chosen to have points that coincide with the measurement grid as well as extra intermediate points.

The AKs, calculated on a fine grid of 1 km for both NRT and OL measurements, as well as the profiles corresponding to the atmospheric status for which **A** has been calculated, are available on the web at http://www.ifac.cnr.it/retrieval/auxiliary.html.

From the atmospheric status it is possible to derive the pressure grid for which the AKs are calculated. However, this is the pressure grid of a nominal measurement and is in general different from that of a real measurement.

For small differences in the measurement grid, the shape of the AK depends more on the relative location of the measurement points than on their actual altitude. Therefore, the AKs calculated for a nominal measurement grid can be used to define the AKs of the real measurement grid. Namely, the measured tangent pressure can be associated with the values of the AKs at the measurement grid. This implies a stretching/shrinking of the representation grid and an interpolation is needed for the determination of the pressure of the intermediate points. Assuming a logarithmic variation of pressure with altitude, if $\boldsymbol{p}_{\mathrm{nom}}$ and $\boldsymbol{p}_r$ are the pressure of the nominal and real pressure grid respectively, the pressure of the intermediate point can be determined from the following

expression:

$$\ln \boldsymbol{p}_r\,(i+j) = \ln \boldsymbol{p}_r\,(i) + \frac{\left(\ln \frac{\boldsymbol{p}_r(i+n)}{\boldsymbol{p}_r(i)}\right)}{\left(\ln \frac{\boldsymbol{p}_{\mathrm{nom}}(i+n)}{\boldsymbol{p}_{\mathrm{nom}}(i)}\right)} \ln \frac{\boldsymbol{p}_{\mathrm{nom}}\,(i+j)}{\boldsymbol{p}_{\mathrm{nom}}\,(i)}, \tag{10}$$

where i is the index of a measurement grid point, $(n-1)$ is the number of intermediate points, $i+n$ is the index of the next measurement grid point and $j=1$, $n-1$ is the index of the intermediate grid point.

Outside the retrieval range:

$$\boldsymbol{p}_r\,(l) = \boldsymbol{p}_{\mathrm{nom}}\,(l)\,\frac{\boldsymbol{p}_r\,(k)}{\boldsymbol{p}_{\mathrm{nom}}\,(k)}, \tag{11}$$

where l is the index of the extrapolated point and $\boldsymbol{p}_r$(k) and $\boldsymbol{p}_{\mathrm{nom}}$(k) are the pressure of the highest/lowest retrieved point in the real and nominal grid, respectively.

This process provides the averaging kernel on an irregular pressure grid that corresponds to the specific limb measurements.

The AKs in the case of ozone retrieval for the 20° N–65° N latitude band in July represented on a grid of 1 km step are shown in Fig. 10.

The AK cannot always be defined. When the AKM is calculated using different "seeds" for the generation of the random errors added to the spectra the same AKMs should be obtained. If different AKMs are obtained it means that the measurement error can change the retrieved values of a large amount and the retrieval of that parameter is ill-conditioned. In these cases, occurring for some of the additional altitudes available in the OL products, the averaging kernels are not provided, stressing that the corresponding retrieved value has no physical meaning and can only be used to characterise the retrieval process from the mathematical point of view.

7 ORM performances

The χ^2–test of each retrieval, given by the value of χ^2 function at convergence (see Eq. 1) divided by the Number of Degrees of Freedom (NDF) can be used as a diagnostic tool for the evaluation of the code performances.

All data measured in the year 2003 that were reprocessed by the ESA OL processor have been used to evaluate the mean χ^2-test value of each orbit. The histograms of the mean χ^2 values for the different species are shown in Fig. 11.

With the only exception of NO_2, that shows occasional large values which are being investigated, the χ^2 of the other species are stable in time.

Table 4 shows for all target species the one-year mean of the measured χ^2 test. Deviations of the χ^2 test from unity provide an indication of the existence of forward model errors even if not all forward model errors do equally manifest themselves through this test. The estimated χ^2 test, calculated from the a priori estimates of forward model and random errors, is also reported in the table.

In general we find that the χ^2 test does not differ much from unity and that a good agreement is obtained between measured and estimated values. For most retrievals, the measured χ^2 are smaller than the calculated ones confirming that conservative estimates of the forward model errors are currently made. An exception is observed in the already mentioned case of NO_2.

The third row of the table shows the standard deviation of the χ^2 statistics as measured from the one-year distribution. The measured standard deviation is the results of three main contributions: statistical standard deviation, due to the finite number of averaged residuals and equal to $\sqrt{\frac{2}{\mathrm{NDF}}}$, spread in the statistics of the χ^2 test due to forward model errors with variable amplitude and spread associated with convergence criteria. The statistical standard deviation, also reported in the 4th row, is always very small and has a negligible effect.

It has been verified that the spread due to convergence criteria is the main cause of the measured standard deviation for all retrievals except p-T and H_2O retrievals. For

these two retrievals, the presence of forward model errors with variable amplitude has to be considered as the main cause of the measured standard deviation.

The last line of Table 3 shows that a good percentage of retrievals have successfully reached convergence.

8 Example of the results

The polar orbit of the ENVISAT satellite provides a nearly full coverage of the globe in one day. The global coverage, combined with the MIPAS capability of retrieving, simultaneously and during both day and night, the vertical profile of numerous species, allows continuous measurement of the three dimensional (versus latitude, longitude and altitude) atmospheric composition as a function of time. This capability represents a major achievement with respect to previous measurements.

The fact that not only a key constituent is measured, but a set of interlinked species are simultaneously determined is of particular importance from the scientific point of view. As an example of this potentiality of MIPAS measurements a qualitative comparison is shown between the Antarctic ozone holes in 2002 and 2003, that present very different characteristics.

The maps of T, O_3, CH_4 and HNO_3 obtained by ORM from the analysis of a single orbit on 26 September in the two years are shown in Fig. 12.

The maps relative to the year 2002 highlight a strongly perturbed Antarctic stratospheric vortex, due to a major warming which occurred very early that year, while in 2003 at the same date the vortex still appears very stable (as inferred by the temperature map) and with a subsidence extended over a large area (as inferred by the N_2O map). O_3 depletion correlates with denitrification at low altitudes (chemical depletion) and with subsidence at high altitudes (dynamical depletion). The different dynamics and chemistry observed in the two years lead to a significantly different pattern in ozone distribution. The vertically resolved measurements of MIPAS easily highlight the on-going processes and resolve the two regimes of behaviour in the two years. The MI-

PAS observations made during the ozone hole break-up in 2002 are further described in a number of papers, mostly collected on a special issue on Antartic vortex 2002[6].

9 Conclusions

The performances of the level 2 analysis of MIPAS instrument during the first two years of instrument operations have been reviewed. The features of the ORM code, which is the basis of the operational level 2 analysis, have been recalled and the approximations and assumptions, implemented in the code in order to meet the NRT and accuracy requirements, have been critically reviewed testing their impact on the retrieved profiles in the case of real measurements.

The retrieval code has successfully processed, in NRT, MIPAS measurements without any change in the level 2 processor. Changes have only been made in the preprocessor with the addition of an algorithm for the rejection of measurements spoiled by clouds (cloud filtering).

A refinement of both the retrieval settings and the spectroscopic database has proved to be important for the quality of the products. In particular, the convergence error can be reduced using more stringent convergence criteria and the extrapolation error, due to the profile assumptions outside the retrieval range, can be reduced using an extended retrieval range. Unfortunately, these error reductions can only be attained at the expenses of computing time and have not been implemented in the NRT analysis. These improvements have been implemented in the OL products, which have a less stringent constraints for the processing time and are produced some time after the measurement using the same code and better geolocated data.

A review of the total error budget of the retrieved profiles was performed on the basis of the results of instrument and level 1 processor characterisation, and of specific tests made on the level 2 data. The error budget and the overall performances of

[6] J. Atmos. Sci., vol. 62, number 3 (March 2005).

the level 2 processor are verified with a statistical analysis of the mean χ^2-test of the measurements obtained during the first two years of MIPAS operations. We find that in general the chi-square is smaller than our a priori estimate indicating that conservative forward model errors have been assumed. In the error budget the forward model errors are comparable with the random errors as required in an optimized retrieval, however, the total error is larger than the possibilities of the MIPAS instrument. Further work is needed to reduce the amplitude of forward model errors so that the random error can also be reduced with the analysis of more microwindows and a smaller total error is obtained.

Acknowledgements. This study was supported by ESA contracts 11717/95/NL/CN and 17580/03/I-OL. The study team is grateful to H. Nett, J. Langen and R. Koopman for the fruitful discussions and for the efficient coordination of MIPAS NRT code development studies.

References

Birk, M. and Wagner, G.: Radiometric accuracy assessment of MIPAS on ENVISAT, Proceedings of ENVISAT Calibration Review, Nordwick, ESA-ESTEC, ESA Publication SP-520, 2002.

Carlotti, M.: Global-fit approach to the analysis of limb-scanning atmospheric measurements, Appl. Opt., 27, 3250–3254, 1988.

Carlotti, M. and Ridolfi, M.: Derivation of temperature and pressure from submillimetric limb observations, Appl. Opt., 38, 2398–2409, 1999.

Carlotti, M., Dinelli, B. M., Raspollini, P., and Ridolfi, M.: Geo-fit approach to the analysis of limb-scanning satellite measurements, Appl. Opt., 41, 1872–1885, 2001.

Ceccherini, S., Carli, B., Pascale, E., Prosperi, M., Raspollini, P., and Dinelli, B. M.: Comparison of measurements made with two different instruments of the same atmospheric vertical profile, Appl. Opt., 42(32), 6465, 2003.

Chipperfield, M. P.: Multiannual Simulations with a Three-Dimensional Chemical Transport Model, J. Geophys. Res., 104, 1781–1805, 1999.

Clarmann, V. T., Dudhia, A., Echle, G., Flaud, J.-M., Harrold, C., Kerridge, B., Koutoulaki, K.,

Linden, A., Lopez-Puertas, M., Lopez-Valverde, M. A., Martin-Torres, F. J., Reburn, J., Remedios, J., Rodgers, C. D., Siddans, R., Wells, R. J., and Zaragoza, G.: Study on the simulation of atmospheric infrared spectra, Tech. Rep., Final Report of ESA Contract 12054/96/NL/CN, European Space Agency, ESTEC, Noorwijk, The Netherlands, 1998.

Clarmann., v. T., Ceccherini, S., Doicu, A., Dudhia., A., Funke, B., Grabowski, U., Hilgers, S., Jay, V., Linden, A., Lopez-Puertas, M., Martin-Torres, F. J., Payne, V., Reburn, J., Ridolfi, M., Schreier, F., Schwarz, G., Siddans, R., and Steck, T.: A blind test retrieval experiment for infrared limb emission spectroscopy, J. Geophys. Res., 108(D23), 4746, 2003a.

Clarmann, v. T., Glatthor, N., Grabowski, U., Höpfner, M., Kellmann, S., Kiefer, M., Linden, A., Mengistu Tsidu, G., Milz, M., Steck, T., Stiller, G. P., Wang, D. Y., Fischer, H., Funke, B., Gil-López, S., and López-Puertas, M.: Retrieval of temperature and tangent altitude pointing from limb emission spectra recorded from space by the Michelson Interferometer for Passive Atmospheric Sounding (MIPAS), J. Geophys. Res., 108(D23), 4736, doi:10.1029/2003JD003602, 2003b.

Clarmann, v. T., Höpfner, M., Funke, B., López-Puertas, M., Dudhia, A., Jay, V., Schreier, F., Ridolfi, M., Ceccherini, S., Kerridge, B. J., Reburn, J., Siddans, R., and Flaud, J.-M.: Modelling of atmospheric mid-infrared radiative transfer: the AMIL2DA algorithm intercomparison experiment, J. Quant. Spectr. Radiat. Trans., 78, 3–4, 381, 2003c.

Dudhia, A.: REC analysis of MIPAS data, Technical Note, of ESA Contract no. 11717/95/NL/CN, 2002.

Dudhia, A., Jay, V. L., and Rodgers, C. D.: Microwindow selection for high-spectral-resolution sounders, App. Opt., 41, 3665–3673, 2002a.

Dudhia, A., Morris, P. E., and Wells, R. J.: Fast monochromatic radiative transfer calculations for limb sounding, J. Quant. Spectr. Radiat. Trans., 74, 745–756, 2002b.

Edwards, P.: High Level algorithm definition document of the MIPAS Reference Forward Model, ESA Report PO-TN-OXF-GS-0004, 1997.

Edwards, D. P. and Strow, L. L.: Spectral line shape considerations for limb temperature sounders, J. Geophys. Res., 96, 20 859–20 868, 1991.

Fischer, H., Blom, C., Oelhaf, H., Carli, B., Carlotti, M., Delbouille, L., Ehhalt, D., Flaud, J.-M., Isaksen, I., Lopez-Puertas, M., McElroy, C. T., and Zander, R.: Envisat-MIPAS – An instrument for atmospheric chemistry and climate research, edited by: Readings, C. and Harris, R. A., ESA Publication SP-1229, European Space Agency, 2000.

Flaud, J. M. and Piccolo, C.: Spectroscopic Database Updates, Technical Note of the ESA

study no. 11717/95/NL/CN, July 2001.

Flaud, J. M. and Piccolo, C.: MIPAS_03: an update of the MIPAS.PF2 database, September 2003, Technical Note of the ESA study no. 11717/95/NL/CN., 2003.

Flaud, J.-M., Perrin, A., Orphal, J., Kou, Q., Flaud, P.-M., Dutkiewicz, Z., and Piccolo, C.: New analysis of the u5+u9−u9 hot band of HNO_3, J. Quant. Spectr. Radiat. Trans., 77, 355–364, 2003a.

Flaud, J.-M., Piccolo, C., Carli, B., Perrin, A., Coudert, L. H., Teffo, J.-L., and Brown, L. R.: Molecular line parameters for the MIPAS (Michelson Interferometer for Passive Atmospheric Sounding) experiment, J. Atmos. Ocean Optics, 16, 172–182, 2003b.

Flaud, J.-M., Wagner, G., Birk, M., Camy-Peyret, C., Claveau, C., De Backer-Barilly, M. R., Barbe, A., and Piccolo, C.: The Ozone absorption around 10 mm, J. Geophys. Res.-Atmos., 108(D9), 4269, 2003c.

Friedl-Valloon, F., Maucher, G., Seefeldner, M., Trieschmann, O., Kleinert, A., Lengel, A., Keim, C., Oelhaf, H., and Fischer, H.: Design and characterisation of the balloon-borne Michelson Interferometer for Passive Atmospheric Sounding (MIPAS-B2), Appl. Opt., 43, 3335–3355, 2004.

Funke, B., López-Puertas, M., Clarmann, v. T., Stiller, G. P., Fischer, H., Glatthor, N., Grabowski, U., Höpfner, M., Kellmann, S., Kiefer, M., Linden, A., Mengistu Tsidu, G., Milz, M., Steck, T., and Wang, D. Y.: Retrieval of stratospheric NO and NO2 from 5.3 and 6.2 μm non-LTE emissions measured by MIPAS on ENVISAT, J. Geophys. Res., 110, D09302, doi:10.1029/2004JD005225, 2005.

Garcia-Comas, M., López-Puertas, M., Mertens, C. J., Wintersteiner, P. P., Picard, R. H., Winick, J. R., Mlynczak, M. G., Remsberg, E. E., Russell III, J. M., and Gordley, L. L.: Comparisons of SABER non-LTE retrievals of kinetic temperature with ground-based measurements, Geophys. Res. Abstr., 5, 10 148, 2003.

Greenhough, J., Remedios, J. J., Sembhi, H., and Kramer, L. J.: Towards cloud detection and cloud frequency distributions from MIPAS infra-red observations, Adv. Space Res., 36, 800–806, 2005.

Hauglustaine, D. A., Brasseur, G. P., Walters, S., Rasch, P. J., Müller, J.-F., Emmons, L. K., and Carroll, M. A.: MOZART, a global chemical transport model for ozone and evaluation, J. Geophys. Res., 28 291–28 335, 1998.

Höpfner, M., Oelhaf, H., Wetzel, H., Friedl-Valloon, F., Glatthor, N., Stiller, G. P., von Clarmann, T., Fischer, H., Kröger, C., and Deshler, T.: Evidence of scattering of tropospheric radiation by

PSCs in mid-IR emission spectra: MIPAS-B observations and KOPRA simulations, Geophys. Res. Lett., 29, 1278, doi:10.1029/2001GL014443, 2002.

Höpfner, M., Luo, B. P., Massoli, P., Cairo, F., Spang, R., Snels, M., Di Donfrancesco, G., Stiller, G., v. Clarmann, T., Fischer, H., and Biermann, U.: Spectroscopic evidence for β-NAT, STS and ice in MIPAS infrared limb emission measurements of polar stratospheric clouds, Atmos. Chem. Phys., 6, 1201–1219, 2006.

Kalman, R. E.: Algebraic aspects of the generalized inverse of a rectangular matrix, Proc. of Advanced Seminar on Generalized Inverse and Applications, edited by: Nashed, M. Z., Academic, San Diego, Calif., 111–124, 1976.

Levenberg, K.: A method for the solution of certain problems in least squares, Quart. Appl. Math., 2, 164–168, 1944.

López-Puertas, M., Funke, B., García-Comas, M., López-Valverde, M. A., Martín-Torres, J.: Advanced MIPAS Level 2 Data Analysis (AMIL2DA), Project EVG1-CT-1999-00015, Report on the Climatology of Vibrational Temperatures, March 2002.

López-Puertas, M., Koukouli, M. E., Funke, B., Gil-López, S., Glatthor, N., Grabowski, U., Stiller, G. P., and Clarmann, v. T.: Evidence for CH4 7.6 μm non-local thermodynamic equilibrium emission in the mesosphere, Geophys. Res. Lett., 32, L04805, doi: 10.1029/2004GL021641, 2005.

Marquardt, D. W.: An algorithm for the least-squares estimation of non-linear parameters, SIAM J. Soc. Appl. Math. 11, 431, 1963.

Mencaraglia, F., Bianchini, G., Boscaleri, A., Carli, B., Ceccherini, S., Raspollini, P., Flaud, J.-M., and Perrin, A.: Validation of MIPAS satellite measurements of HNO3 with comparison of rotational and vibrational spectroscopy, J. Geophys. Res., in press, 2006.

Menke, W.: Geophysical Data Analysis: Discrete Inverse Theory, Academic, San Diego, California, 1984.

Nett, H. and Perron, G.: ENVISAT-MIPAS: instrument commissioning & early results, Geoscience and Remote Sensing Symposium, 2002, IGARSS '02, 2002 IEEE International, 1, 602–604, 2002a.

Nett, H., Perron, G., Sanchez, M., Burgess, A., and Mosner, P.: MIPAS In-Flight Calibration and Processor Verification, Proceedings of ENVISAT Calibration Review, Nordwick, ESA-ESTEC, ESA Publication SP-520, 2002b.

Norton, R. H. and Beer, R.: New apodizing functions for Fourier spectroscopy, J. Opt. Soc. Am., 66, 259–264, 1976; errata corrige J. Opt. Soc. Am., 67, 419, 1977.

Piccolo, C., Carli, B., and Ceccherini, S.: Test of the MIPAS retrieval code with ATMOS measurements, J. Atmos. Oceanic Technol., 21(10), 1557–1565, 2004.

Raspollini, P. and Ridolfi, M.: Mapping of Temperature and Line-of-Sight Errors in Constituent Retrievals for MIPAS/ENVISAT Measurements, Atmos. Environ., 34, 5329–5336, 2000.

Remedios, J. J.: Extreme Atmospheric Constituent Profiles for MIPAS, Proceedings of the European symposium on atmospheric measurements from space, ESTEC, Netherlands, 20–22 January, 2, 779–783, 1999.

Ridolfi, M.: Characterisation of MIPAS Line of Sight (LOS) pointing error, TN contract ESA ESRIN no. 17580, 2005.

Ridolfi, M., Carli, B., Carlotti, M., von Clarmann, T., Dinelli, B. M., Dudhia, A., Flaud, J.-M., Höpfner, M., Morris, P. E., Raspollini, P., Stiller, G., and Wells, R. J.: Optimized forward model and retrieval scheme for MIPAS near-real-time data processing, Appl. Opt., 39, 1323–1340, 2000.

Ridolfi, M., Ceccherini, S., and Carli, B.: Optimal interpolation method for intercomparison of atmospheric measurements, Opt. Lett., 31, 855–857, 2006.

Rodgers, C. D.: Inverse methods for atmospheric sounding – Theory and practise, edited by: Taylor, F. W., World Scientific, 2000.

Rodgers, C. D. and Connor, B. J.: Intercomparison of remote sounding instruments, J. Geophys. Res., 108, 4116–4130, 2003.

Rosenkranz, P. W.: Shape of the 5 mmoxygen band in the atmosphere, IEEE Trans. Antennas Prop. AP-23, 498–506, 1975.

Rothman, L. S., Rinsland, C. P., Goldman, A., Massie, S. T., Edwards, D. P., Flaud, J.-M., Perrin, A., Camy-Peyret, C., Dana, V., Mandin, J.-Y., Schroeder, J., McCann, A., Gamache, R. R., Wattson, R. B., Yoshino, K., Chance, K. V., Jucks, K. W., Brown, L. R., Nemtchinov, V., and Varanasi, P.: The HITRAN Molecular Spectroscopic Database and HAWKS (HITRAN Atmospheric WorKStation): 1996 Edition, J. Quant. Spectr. Radiat. Trans., 60, 665, 1998.

Sivia, D. S.: Data analysis. A Bayesian tutorial, Clarendon Press – Oxford, 1998.

Spang R., Remedios, J. J., and Barkley, M. P.: Colour indices for the detection and differentiation of cloud types in infra-red limb emission spectra, Adv. Space Res., 33, 7, 1041–1047, 2004.

Spang, R., Eidmann, G., Riese, M., Preusse, P., Offermann, D., Pfister, L., and Wang, P. H.: CRISTA observations of cirrus clouds around the tropopause, J. Geophys. Res., 107(D23), 8174, doi:10/1029/2002JD000698, 2002.

Spang, R. and Remedios, J. J.: Observations of a distinctive infra-red spectral feature in the atmospheric spectra of polar stratospheric clouds measured by the CRISTA instrument, Geophys. Res. Lett., 30(16), 1875, 2003.

Verronen, P. T., Kyrölä, E., Tamminen, J., Funke, B., Gil-López, S., Kaufmann, M., López-Puertas, M., Clarmann, T. v., Stiller, G., Grabowski, U., and Höpfner, M.: A comparison of night-time GOMOS and MIPAS ozone profiles in the stratosphere and mesosphere, Adv. Space Res., 36, 958–966, 2005.

Table 1. List of nominal microwindows.

Microwindow label	Spectral range	Altitude range
P, T retrieval		
PT_..039	685.7000–685.8250 cm^{-1}	33.0–47.0 km
PT_..001	686.4000–689.4000 cm^{-1}	30.0–68.0 km
PT_..037	694.8000–695.1000 cm^{-1}	27.0–36.0 km
PT_..038	700.4750–701.0000 cm^{-1}	21.0–30.0 km
PT_..004	728.3000–729.1250 cm^{-1}	15.0–27.0 km
PT_..006	741.9750–742.2500 cm^{-1}	15.0–24.0 km
PT_..002	791.3750–792.8750 cm^{-1}	6.0–33.0 km
H_2O retrieval		
H2O_.002	807.8500–808.4500 cm^{-1}	12.0–18.0 km
H2O_.022	946.6500–947.7000 cm^{-1}	6.0–18.0 km
H2O_.007	1645.5250–1646.2000 cm^{-1}	27.0–60.0 km
H2O_.001	1650.0250–1653.0250 $cm^{-}1$	15.0–68.0 km
O_3 retrieval		
O3_..021	763.3750–766.3750 cm^{-1}	6.0–68.0 km
O3_..013	1039.3750–1040.3250 cm^{-1}	52.0–68.0 km
O3_..001	1122.8000–1125.8000 cm^{-1}	6.0–68.0 km
HNO_3 retrieval		
HNO3_001	876.3750–879.3750 cm^{-1}	6.0–68.0 km
HNO3_006	885.1000–888.1000 cm^{-1}	6.0–42.0 km
CH_4 retrieval		
CH4_.012	1227.1750–1230.1750 cm^{-1}	6.0–60.0 km
CH4_.001	1350.8750–1353.8750 cm^{-1}	12.0–68.0 km
N_2O retrieval		
N2O_.012	1233.2750–1236.2750 cm^{-1}	6.0–27.0 km
N2O_.001	1272.0500–1275.0500 cm^{-1}	12.0–60.0 km
NO_2 retrieval		
NO2_.001	1607.2750–1610.2750 cm^{-1}	15.0–68.0 km
NO2_.003	1613.7250–1616.6000 cm^{-1}	15.0–68.0 km
NO2_.013	1622.5500–1623.4750 cm^{-1}	6.0–30.0 km

Table 2. Altitude retrieval range for the different species in both NRT and OL products.

	Retrieval range for NRT	Retrieval range for OL
PT	12–68 km	6–68 km
H_2O	12–60 km	6–68 km
O_3	12–60 km	6–68 km
HNO_3	12–42 km	9–42 km
CH_4	12–60 km	6–68 km
N_2O	12–47 km	6–60 km
NO_2	24–47 km	24–68 km

Table 3. MIPAS forward model error sources and their amplitudes.

Error Source	1 σ	Name [3]
Errors in Instrument Characterisation		
Radiometric Gain	±2%	GAIN
Spectral Calibration	±0.001 cm^{-1}	SHIFT
Apodised ILS Width	±2%	SPREAD
Errors in radiative transfer parameters		
Profiles of the 6 target gases	±10%	[gas]
Profiles of 22 unretrieved gases	Climatological St. Dev.	[gas]
High Altitude Column	Climatological St. Dev.	HIALT
Spectral database errors	[1]	SPECDB
Error profiles of retrieved p and T	Random covariance [2]	PT
Deficiencies in radiative transfer		
Non-LTE effects	Modelled	NONLTE
CO_2 Line Mixing	Modelled	CO2MIX
Horizontal Temperature gradients	±1 K/100 km	GRA

[1] Based on assumed 1 σ accuracies in line position, strength and halfwidth relative to HITRAN 96 database (Flaud, private communications).
[2] VCM of the pT retrieval error.
[3] "Name" is used in the legends of Figs. 4 and 5.

Table 4. Statistics of ORM performances.

	PT	H_2O	O_3	HNO_3	CH_4	N_2O	NO_2
Measured mean χ^2-test	2.09	1.03	1.34	1.37	1.12	1.25	2.22
Estimated χ^2-test	2.82	1.76	1.79	1.11	2.23	1.27	1.23
Measured standard deviation	0.72	0.36	0.44	0.39	0.30	0.52	2.03
Statistical standard deviation (due to measurement error only)	0.05	0.035	0.03	0.03	0.03	0.035	0.03
% of successful retrievals	95.5	93.2	93.7	94.1	94.5	94	87

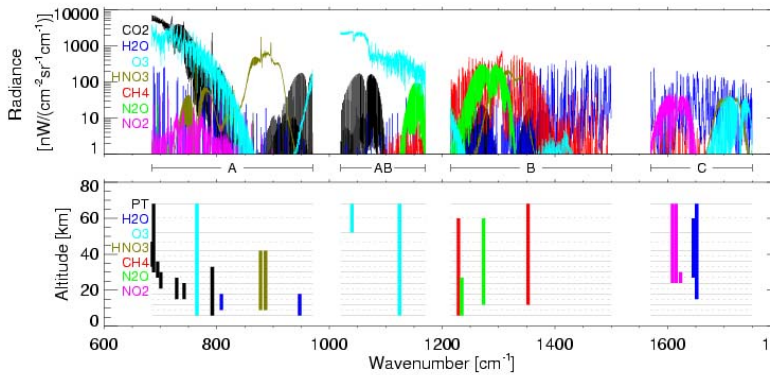

Fig. 1. The upper plot shows the major absorbing molecules in the MIPAS spectra for 21 km tangent altitude and the lower plot shows the spectral locations and tangent altitude range of the microwindows used for the MIPAS retrievals (note that the actual spectral width of each microwindow – maximum 3 cm^{-1} – is too narrow to be shown to scale on these plots).

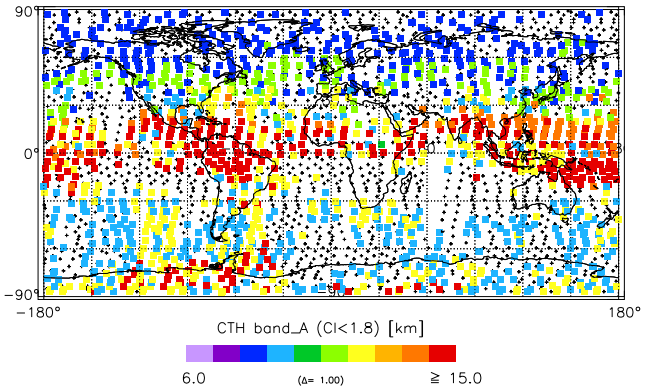

Fig. 2. Global cloud top height map from MIPAS data (OL data) for three days from 15 September 2002. Plus signs (+) indicate limb scans for which no clouds were found, i.e. the entire profile was cloud free. The highest cloud heights are found, as expected, in the tropical upper troposphere (sub-visible cirrus) and in the Antarctic polar vortex (polar stratospheric clouds or PSCs). The PSCs in this period were the final ones observed prior to the unusually early break-up of the vortex in that year. This figure was kindly provided by J. Greenhough.

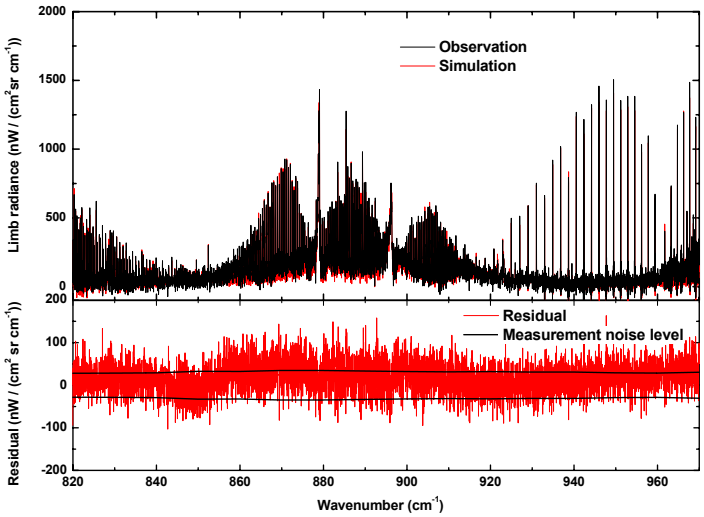

Fig. 3. Comparison between measurements and radiative transfer calculations in a spectra interval of band A that contains the HNO_3 bands (two interacting HNO_3 cold bands ν_5 and $2\nu_9$ centered at 879.109 and 896.448 cm^{-1}, respectively, and two hot bands $\nu_5-\nu_9+\nu_9$ and $3\nu_9-\nu_9$ located at 885.424 and 830.6 cm^{-1}, respectively). Measured limb-radiances at 24 km tangent height (black) and corresponding simulation with the "mipas_pf3.1" spectroscopic line data (red) are shown in the top panel. The difference between the two spectra is shown by the red curve in the bottom panel, together with the specified measurement noise level in this spectral interval (black lines).

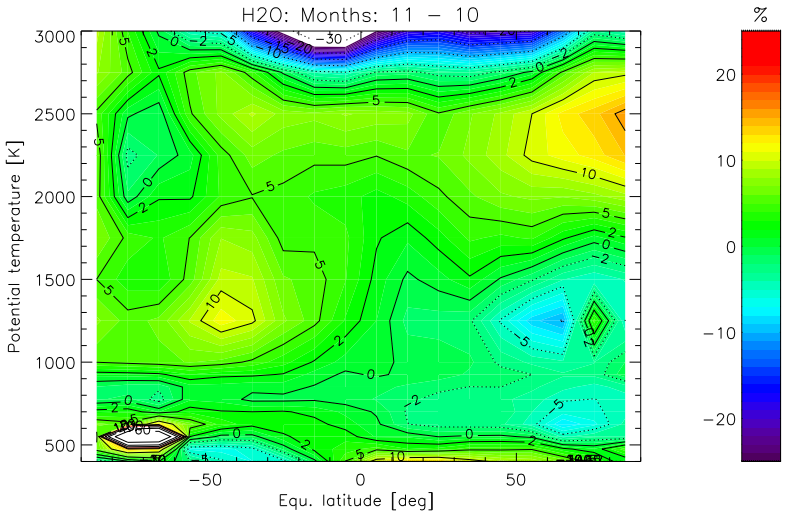

Fig. 4. Day–Night differences in retrieved H_2O on equivalent latitudes versus potential temperature. Differences represent mean values over the whole observational period (July 2002–March 2003).

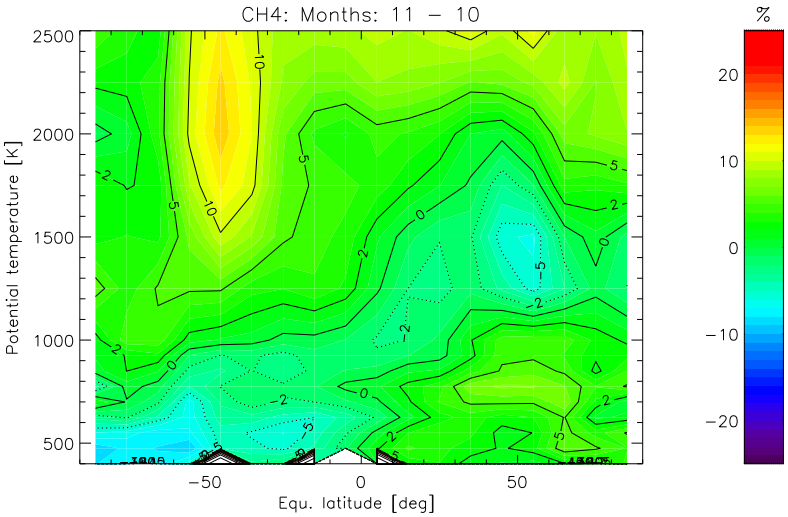

Fig. 5. Day–Night differences in retrieved CH_4 on equivalent latitudes versus potential temperature. Differences represent mean values over the whole observational period (July 2002–March 2003).

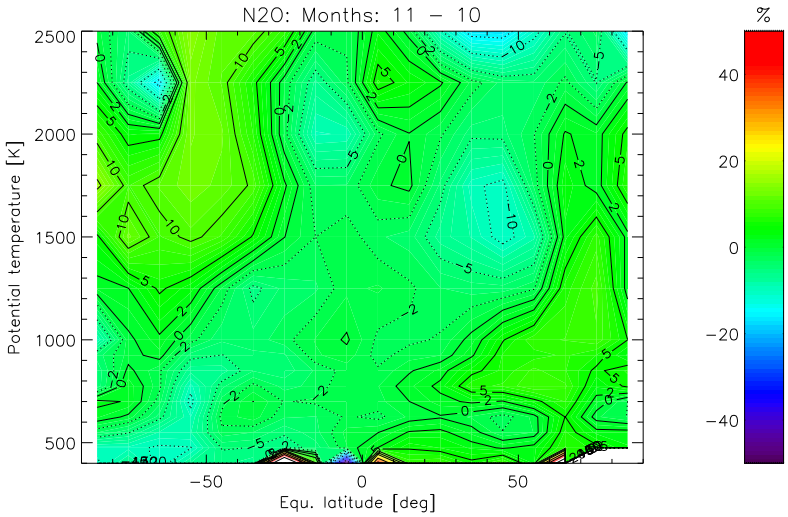

Fig. 6. Day–Night differences in retrieved N_2O on equivalent latitudes versus potential temperature. Differences represent mean values over the whole observational period (July 2002–March 2003).

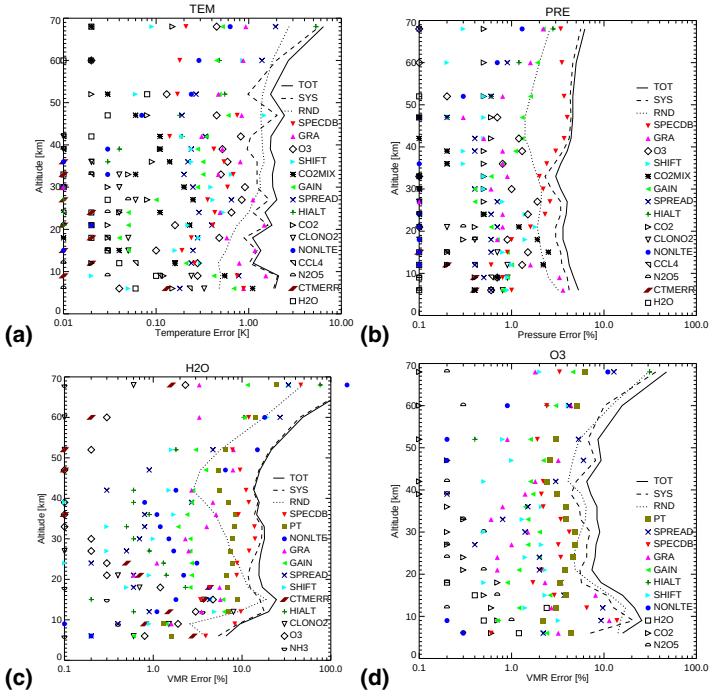

Fig. 7. Error budgets for the MIPAS retrievals of temperature, pressure, water vapour and ozone computed are for midlatitude daytime conditions. The solid line is the Total Error (or Accuracy), represented by the rootsumsquare of the Random Error (or Precision), shown as the dotted line, and the forward model errors, shown as the dashed line. The forward model error is itself the rootsumsquare of the various components shown by different symbols (see Table 3 for details).

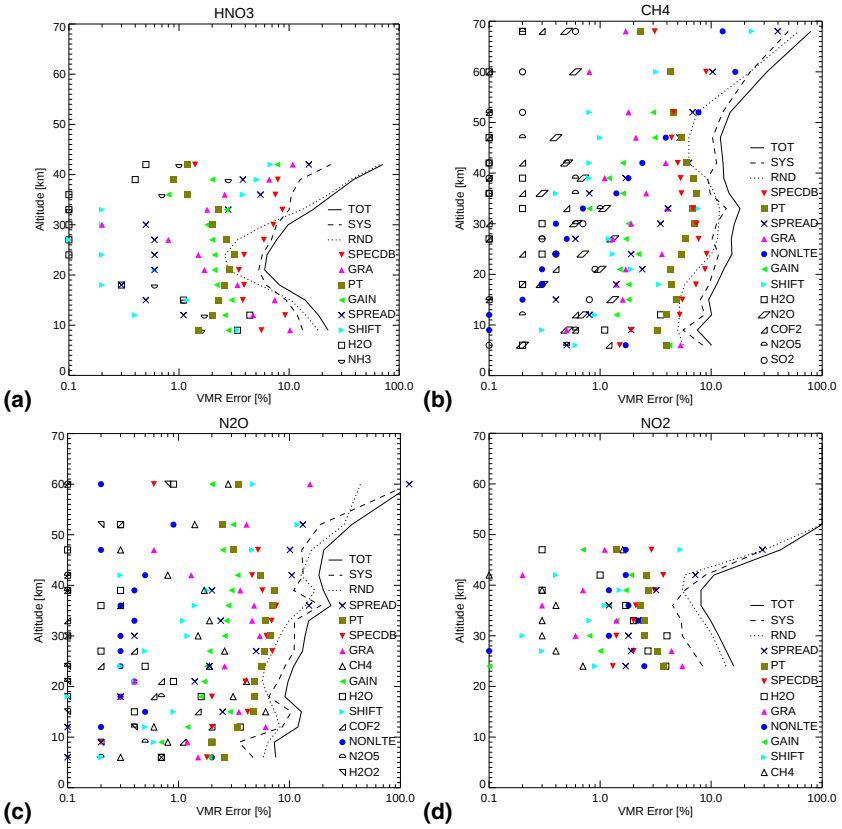

Fig. 8. As Fig. 7, showing retrieval error budgets for nitric acid, methane, nitrous oxide and nitrogen dioxide.

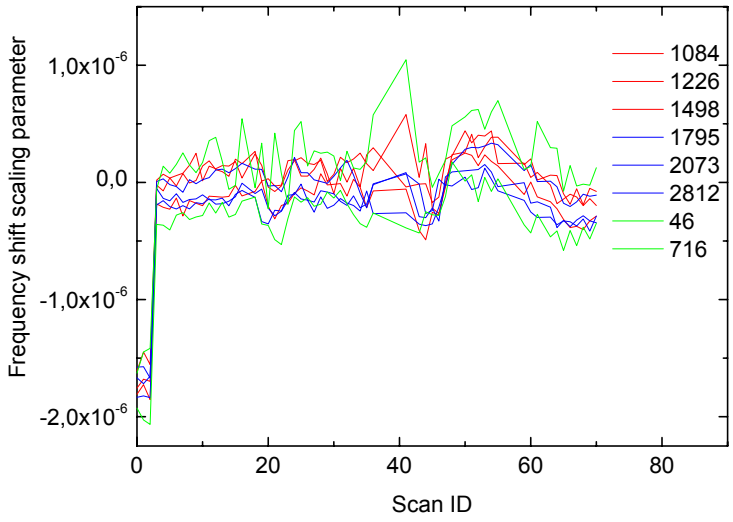

Fig. 9. Fit of the frequency scaling factor as a function of the scan identification number (ID) for different sets of spectral points (depending on the analysed species and on the measurement band). Different colours are used for the fits that use few points (green curves), medium number of points (red curves) and large number of points (blue curves).

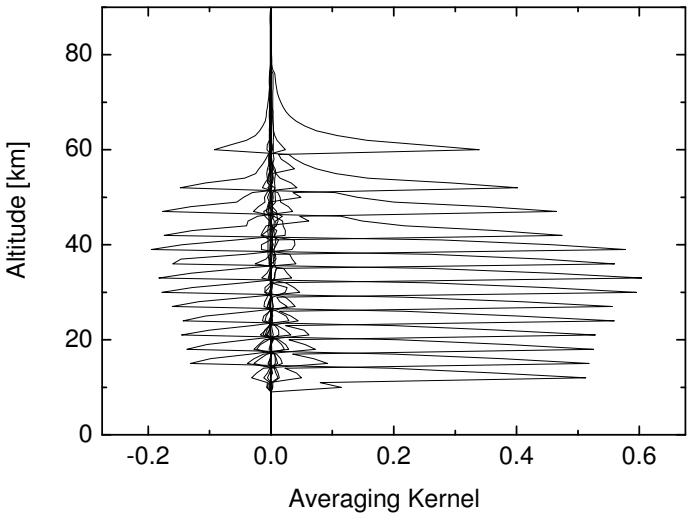

Fig. 10. Averaging kernels for the ozone retrieval in the case of 20° N–65° N latitude band in July.

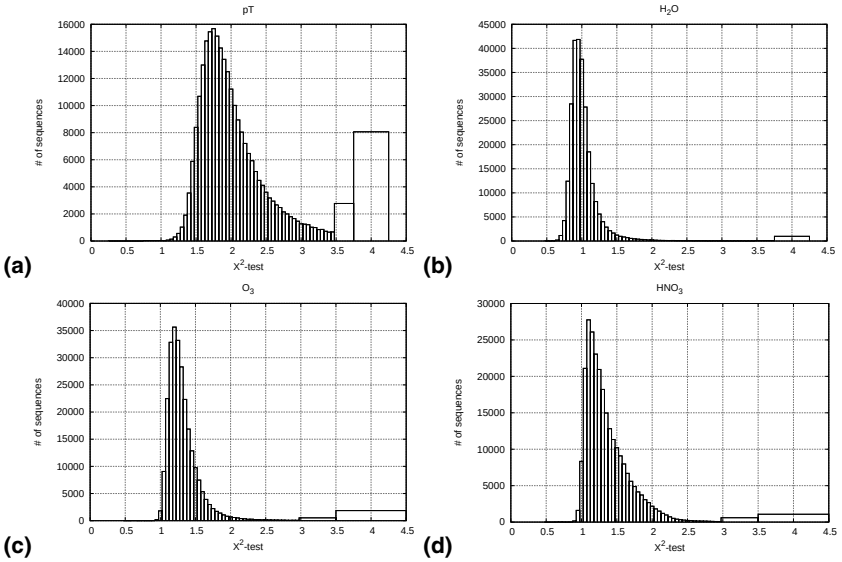

Fig. 11. Histograms of χ^2 test distribution for the different target species.

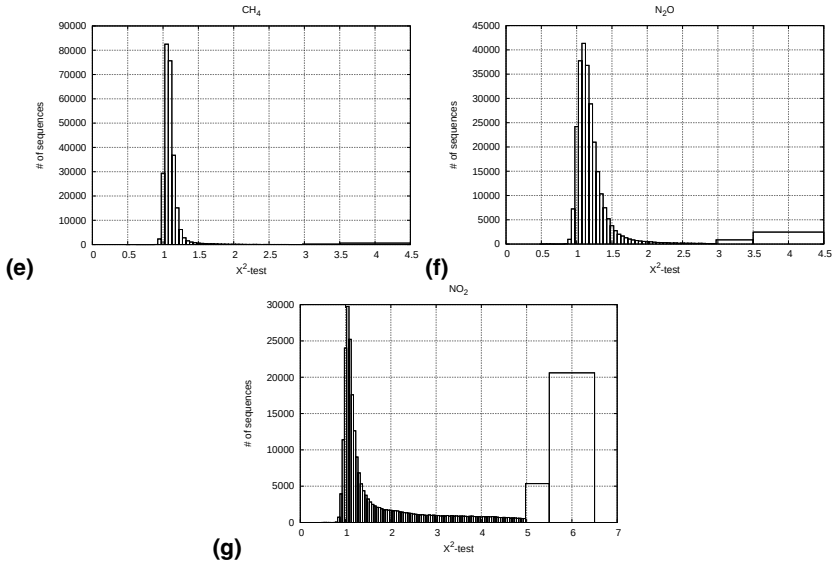

Fig. 11. Continued.

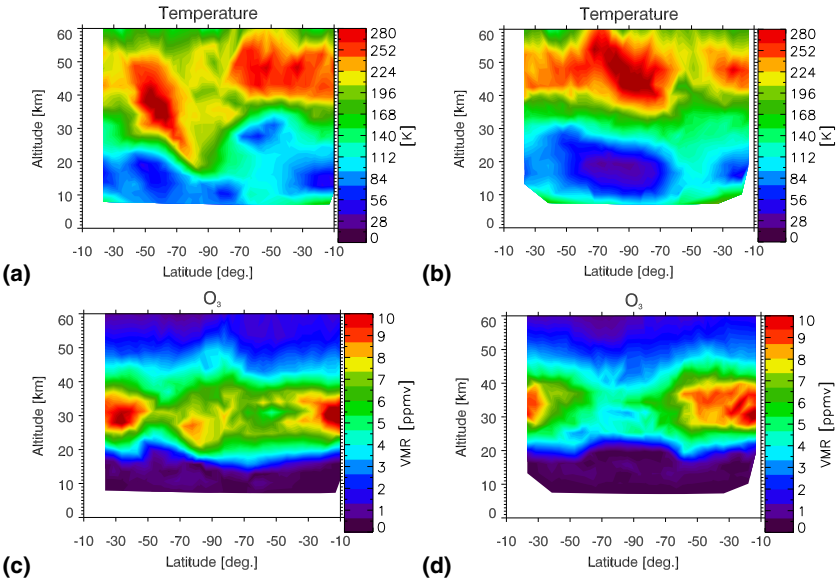

Fig. 12. Maps of temperature and VMR profiles of O_3, HNO_3 and N_2O located around South Pole obtained from the analysis of two orbits measured on 26 September 2002 (maps on the left) and 26 September 2003 (maps on the right), respectively.

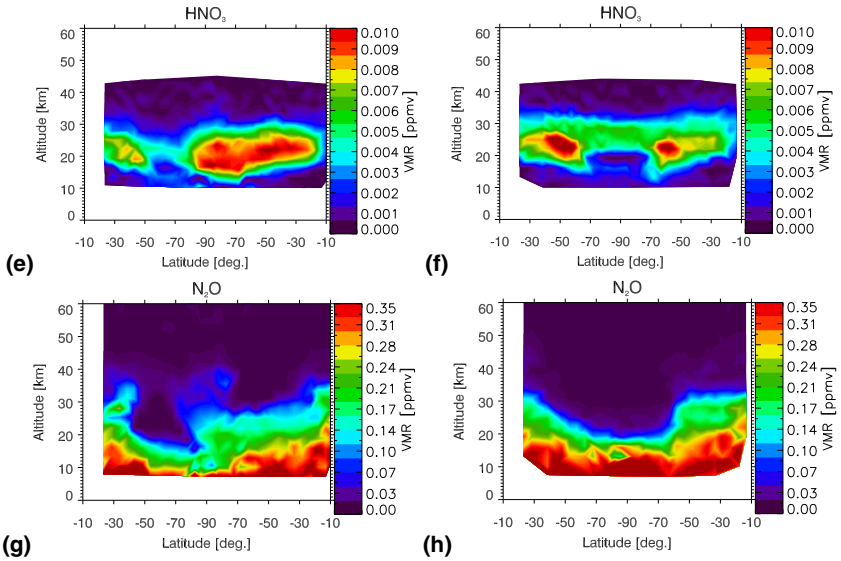

Fig. 12. Continued.